

A multifold reduction in the transition Reynolds number, and ultra-fast mixing, in a micro-channel due to a dynamical instability induced by a soft wall

M. K. S. Verma and V. Kumaran[†]

Department of Chemical Engineering, Indian Institute of Science, Bangalore 560 012, India

(Received 21 February 2013; revised 21 February 2013; accepted 20 May 2013;
first published online 26 June 2013)

A dynamical instability is observed in experimental studies on micro-channels of rectangular cross-section with smallest dimension 100 and 160 μm in which one of the walls is made of soft gel. There is a spontaneous transition from an ordered, laminar flow to a chaotic and highly mixed flow state when the Reynolds number increases beyond a critical value. The critical Reynolds number, which decreases as the elasticity modulus of the soft wall is reduced, is as low as 200 for the softest wall used here (in contrast to 1200 for a rigid-walled channel). The instability onset is observed by the breakup of a dye-stream introduced in the centre of the micro-channel, as well as the onset of wall oscillations due to laser scattering from fluorescent beads embedded in the wall of the channel. The mixing time across a channel of width 1.5 mm, measured by dye-stream and outlet conductance experiments, is smaller by a factor of 10^5 than that for a laminar flow. The increased mixing rate comes at very little cost, because the pressure drop (energy requirement to drive the flow) increases continuously and modestly at transition. The deformed shape is reconstructed numerically, and computational fluid dynamics (CFD) simulations are carried out to obtain the pressure gradient and the velocity fields for different flow rates. The pressure difference across the channel predicted by simulations is in agreement with the experiments (within experimental errors) for flow rates where the dye stream is laminar, but the experimental pressure difference is higher than the simulation prediction after dye-stream breakup. A linear stability analysis is carried out using the parallel-flow approximation, in which the wall is modelled as a neo-Hookean elastic solid, and the simulation results for the mean velocity and pressure gradient from the CFD simulations are used as inputs. The stability analysis accurately predicts the Reynolds number (based on flow rate) at which an instability is observed in the dye stream, and it also predicts that the instability first takes place at the downstream converging section of the channel, and not at the upstream diverging section. The stability analysis also indicates that the destabilization is due to the modification of the flow and the local pressure gradient due to the wall deformation; if we assume a parabolic velocity profile with the pressure gradient given by the plane Poiseuille law, the flow is always found to be stable.

Key words: instability, microfluidics, transition to turbulence

[†] Email address for correspondence: kumaran@chemeng.iisc.ernet.in

1. Introduction

Flows in many microfluidic devices made of soft materials such as polymer gels take place through conduits with flexible walls. In these flows, the effect of wall flexibility on the transition is of fundamental importance with significant technological implications. In typical microfluidic systems, the flow is laminar because the Reynolds number is small in channels/tubes of submillimetre dimensions. Mixing takes place due to molecular diffusion, which is a very slow process. For small molecules in water with diffusion coefficients of around $10^{-9} \text{ m}^2 \text{ s}^{-1}$, it takes 10^3 s to diffuse across a distance of 1 mm. Such long diffusion times limit the feasibility of micro-scale devices for rapid synthesis and processing applications. It is of interest to examine whether a soft wall can enhance mixing by reducing the transition Reynolds number.

Several strategies have been proposed for increasing mixing in micro-reactors. These can be broadly classified into passive strategies where the flow is steady but the streamlines are curved, and active strategies where time dependence is introduced into the flows by external actuation. Passive mixers rely on generating complex flow pathways with curved streamlines, where fluid elements are stretched and rotated along different directions in order to increase the area for mixing. These include channels with repeated bends to curve the streamlines (Liu *et al.* 2000; Jiang *et al.* 2004; Kane *et al.* 2008), wall grooves to introduce secondary flows (Stroock *et al.* 2002), hydrodynamic focusing where inlet streams with very different flow rates come into contact (Knight *et al.* 1998; Ganan-Calvo *et al.* 2011), split-and-recombine strategies (splitting the inlet into a large number of small streams using channel bifurcations and then recombining them by an inverse bifurcation) either in parallel (Bessoth, de Mello & Manz 1999) or in series (Lee *et al.* 2006), and chaotic advection inside microdroplets. Active strategies include pressure pulsing (Glasgow & Aubry 2003), electro-kinetic disturbances induced due to fluctuating electric fields (Bazant & Squires 2004; Posner & Santiago 2006), actuation by acoustic waves (Ahmed *et al.* 2009) and micrometre-sized stirring devices (Mensing *et al.* 2004). In active strategies, there is additional energy input either by micrometre-sized moving parts or by external fields such as electric fields and ultrasound. In passive strategies, there is no external energy input. However, there is an energy cost because the curved streamlines, tortuous paths in split-and-recombine strategies, or secondary flows due to wall grooves, dissipate additional energy due to fluid friction. This results in a higher pressure difference for driving the flow in comparison with a straight micro-channel. These strategies are not amenable to economical scaling-up (or numbering-up) because they involve complicated micro-machining or micrometre-sized moving parts or actuators. Here, we demonstrate an experimental realization of ultra-fast mixing in a micro-channel due to a soft wall. The interaction between the soft wall and the flow results in a dynamical instability, which induces a transition at a Reynolds number much lower than that for the transition in rigid-walled tubes and channels.

For the flow through flexible tubes/channels, previous linear stability studies have shown that the flow does become unstable to infinitesimal disturbances when the Reynolds number exceeds a critical value which could, for sufficiently soft surfaces, be lower than that for the rigid tube/channel transition. The mechanism of instability is not just a modification of the rigid/tube channel instability, but is qualitatively different. There is an instability even at zero Reynolds number, when the dimensionless number $V\eta/GR$ exceeds a critical value (Kumaran, Fredrickson & Pincus 1994; Kumaran 1995), where η is the fluid viscosity, G is the elasticity modulus of the wall material and V and R are the characteristic flow velocity and length. The instability is caused by the shear work at the interface, which transfers energy from the mean flow to

the fluctuations. The transition Reynolds number does depend on the specific type of wall material (Thaokar, Shankar & Kumaran 2001; Chokshi & Kumaran 2008; Gkanis & Kumar 2005; Gaurav & Shankar 2009). Weakly nonlinear studies (Shankar & Kumaran 2001b; Chokshi & Kumaran 2008) indicate that the low-Reynolds-number instability is subcritical.

There are two types of instabilities in the high-Reynolds-number limit, the inviscid and the wall mode instabilities. The effect of viscosity can be neglected in the bulk of the flow in the high-Reynolds-number inviscid instability (Kumaran 1996; Shankar & Kumaran 1999, 2000), although there are boundary layers of thickness $O(Re^{-1/2})$ smaller than the characteristic dimension where viscous effects are important. The transition Reynolds number follows the scaling $Re_t \propto \Sigma^{1/2}$, where $\Sigma = (\rho GR^2/\eta^2)$ is a dimensionless group dependent on material properties and geometry, but independent of flow velocity. Here, ρ is the density of the fluid. The transition is caused by the inertial stresses within the bulk of the flow. In the ‘wall mode’ instability (Kumaran 1998; Shankar & Kumaran 2001a, 2002), there is an energy transfer to perturbations due to the interfacial shear work, which destabilizes the flow when the Reynolds number exceeds a critical value. In this case, there is a boundary layer of thickness $Re^{-1/3}$ at the wall where viscous effects are important, and the transition Reynolds number obeys the scaling law $Re_t \propto \Sigma^{3/4}$. Weakly nonlinear studies have shown that the wall mode instability is supercritical (Chokshi & Kumaran 2009).

The first experiments on the flow through flexible tubes were carried out by Krindel & Silberberg (1979). They considered the fluid flow through a tubular bore in a flexible material (polyacrylamide gel), and measured the pressure drop and flow rate. It was reported that the drag force in a flexible-walled tube is higher than that for a laminar flow for Reynolds numbers as low as 700. However, there has been a subsequent study by Yang *et al.* (2000), using a simulation method developed by Sutterby (1965), which suggested that the higher drag force in Krindel & Silberberg (1979) could be due to a slow convergence of streamlines, rather than a dynamical instability. The low-Reynolds-number instability in the flow past a soft polyacrylamide gel was demonstrated by Kumaran & Muralikrishnan (2000) and Muralikrishnan & Kumaran (2002), and hysteresis and oscillations were also reported by Eggert & Kumar (2004). Shrivastava, Cussler & Kumar (2008) have reported an enhancement in the mass transfer coefficient for transport from the surface due to this instability. The objective in the above-mentioned studies was to verify the viscous instability in the low-Reynolds-number limit, and these were carried out with viscous fluids such as glycerol in a rheometer, in order to achieve a low Reynolds number in flows with a cross-stream length scale of the order of a millimetre. These results are not directly applicable to microfluidic applications where fluids such as water with very low viscosity are used because the Reynolds number could be large, and the neglect of inertial terms in the Navier–Stokes equations is not justified.

A flow instability in a tube of diameter ~ 1 mm was shown by the authors (Verma & Kumaran 2012). A tubular bore in soft polydimethylsiloxane (PDMS) was used for the study, where the PDMS was prepared with a reduced cross-linker concentration to obtain a shear modulus as low as 17 kPa. The transition was detected on the basis of pressure drop measurements, observations of dye-stream breakup as well as wall oscillations by the laser scattering method. The experiments showed that there is an instability of the laminar flow to infinitesimal disturbances for a Reynolds number as low as 500 for tubes of diameter 800 μm and shear modulus 17 kPa. The transition Reynolds number was lower, by a factor of 10, than that predicted for the wall mode

instability by linear stability studies. An important observation was related to the downstream location of the onset of the instability. Downstream from the entrance of the soft section, there is first a divergence (due to the fixed diameter at the entrance) and then a convergence (due to the decrease in pressure with downstream distance). The destabilization of the dye stream was consistently observed in the convergent section of the tube, while the flow in the divergent section was laminar. It was suggested that the flow modification due to the convergence of the tube could result in a mean velocity profile different from the parabolic profile for a cylindrical tube. This modified velocity profile could be destabilized at a lower Reynolds number than the parabolic profile.

The study of Verma & Kumaran (2012) is not of direct relevance to microfluidic applications, since the smallest dimension is ~ 1 mm. Moreover, micro-channels of rectangular cross-section are normally used in microfluidics applications due to the relative ease of fabrication, and the stability limits for a channel flow cannot be directly obtained from tube flow experiments. In the case of rigid-walled conduits, it is known (Drazin & Reid 2004) that the mechanism of instability in a channel (destabilization due to an internal critical layer) is very different from that in a tube (where linear stability analysis predicts the flow is stable at all Reynolds number, but destabilization occurs due to finite-amplitude disturbances). In rigid channels, the experimental transition Reynolds number is much lower than the theoretical predictions based on linear stability analysis. Mechanisms such as transient growth (Trefethen *et al.* 1993; Schmid & Henningson 1994) have been proposed for explaining this difference, and efforts have also been made to detect the finite-amplitude transition threshold in the case of a highly subcritical instability (Hof, Juel & Mullin 2003).

It is important to re-emphasize that there is destabilization due to a linear instability to infinitesimal disturbances in the case of conduits with deformable walls (in contrast to the case of flow through rigid pipes and channels). A second important difference is the possibility of substantial flow modification due to the deformation. Channels and tubes deform very differently under an isotropic pressure. The study of Verma & Kumaran (2012) suggests that tube deformation may be of importance in the transition process, and the effect of deformation in a tube cannot be easily extrapolated to predict the effect of deformation in a channel with a soft wall.

This motivates us to examine whether the flexible-wall instability can be realized in microfluidic applications, and whether this instability could lead to efficient mixing. The experimental techniques for fabricating the channels and determining the transition Reynolds number and mixing efficiency are discussed in the next section. The methods for determining the channel deformation due to an applied pressure gradient are also discussed. Section 3 contains a discussion of the method for determining the velocity profile and pressure gradient in the deformed channels using computational fluid dynamics (CFD) simulations, and the stability analysis of the velocity profiles using the parallel flow approximation. The experimental results for transition (using dye-stream experiments and wall oscillations) and mixing (using image analysis of dye mixing and conductance measurements at the outlet) are presented in § 4. The computation of the flow profiles and pressure drop, and the linear stability analysis of these profiles, are carried out in § 5, and the results are compared with experiments. The main conclusions are presented in § 6.

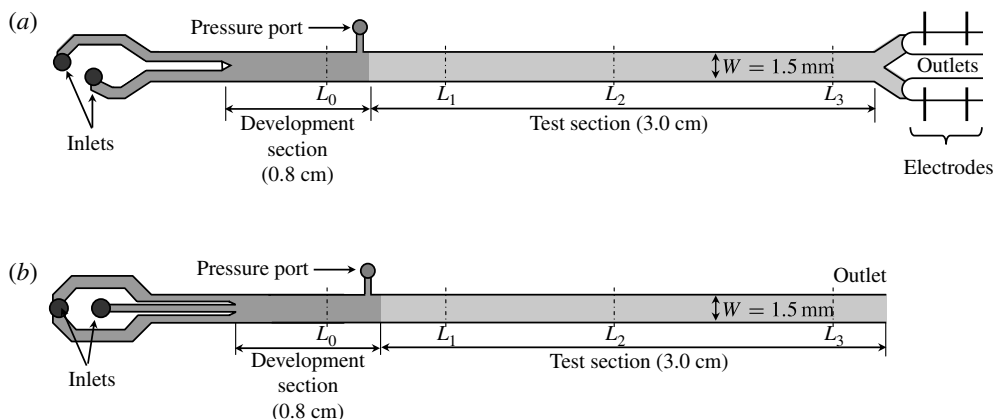


FIGURE 1. Schematic of the micro-channel configuration with the Y inlet (a) and the split inlet (b).

2. Experimental methods

2.1. Micro-channel fabrication

Micro-channels of rectangular cross-section were fabricated in cross-linked PDMS gels (Sylgard 184, Dow Corning) using soft lithography. The width and length of the channels are 1.5 mm and 4 cm, while two different heights, $h_0 = 100$ and $160\ \mu\text{m}$, were used in the experiments. The channels were prepared with three ‘hard’ walls, using the standard 10% catalyst concentration. The fourth wall of the channel was made soft, with a lower catalyst concentration in order to reduce the modulus of elasticity. In the following discussion, a distinction is made between *hard* PDMS, fabricated using the standard catalyst concentration of 10% with a shear modulus of $\sim 0.55\ \text{mPa}$, and *soft* PDMS, in which the catalyst concentration is varied in order to alter the shear modulus. The channel is made of two sections, an upstream developing section of length 0.8 cm with four walls of hard PDMS, to ensure that the flow is fully developed before the fluid enters the test section of length 3 cm with three walls of hard PDMS and one wall of soft PDMS. The details of the procedure are provided in appendix A.

2.2. Channel geometry

Two different channel geometries were used. The first is the Y inlet, shown in figure 1(a), which is used for the mixing experiments. Here, two symmetric inlet streams connected to two syringe pumps, merge together at the entrance of the micro-channel. The flow rates in the two inlets are equal, so that there is no shearing at the interface. In this configuration, there is a symmetric split outlet as well, so that mixing of the two streams at the outlet can be measured using conductance measurements. For this purpose, micro surge tanks were fabricated at the outlet, so that the conductance in the outlet stream can be directly measured. For the Y inlet, the channel height used was $100\ \mu\text{m}$ in all cases. The Y inlet channel cannot be easily used for comparison of the pressure drop with simulations because the surge tanks at the outlet cannot be easily simulated, or for wall oscillations by laser scattering experiments, because one of the fluids is coloured. For this purpose, the second split-inlet configuration was used.

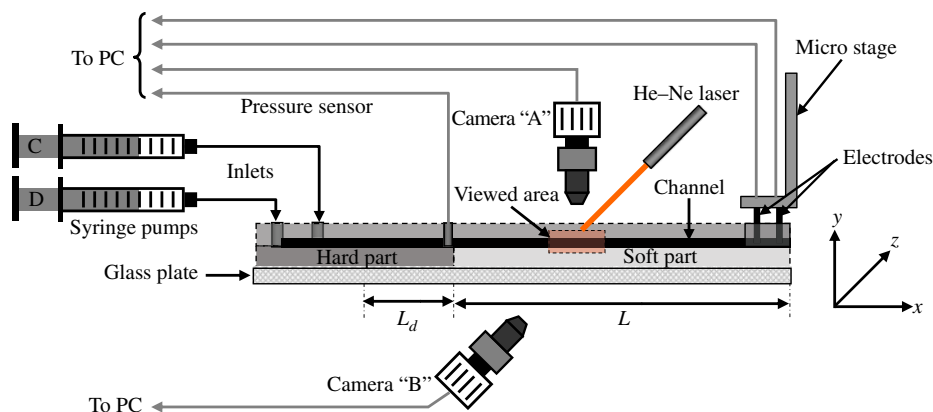


FIGURE 2. (Colour online) Experimental set-up.

The split-inlet channel, shown in figure 1(b) consists of a central core of the channel, of width 0.3 mm, connected to one inlet, while the outer flow on the two sides, of width 0.6 mm each, are split from a second inlet and delivered by symmetric conduits on the two sides of the core. In our dye-stream mixing experiments discussed later, the flow through the central inlet is used for inserting the dye stream, while that from the two sides connected to the split inlet is used for clear fluid. The flow rates in the syringe pumps connected to the core and split inlets are maintained in the ratio 1:5, so that the velocities in the three streams at the entrance to the development section are equal. The split-inlet channels were fabricated with two different channel heights, 100 and 160 μm .

In all cases, the configuration consists of an upstream development section, of length 0.8 cm, with all four walls made of hard gel as described in § 2.1. The development section is followed by a test section of length 3 cm, in which one of the walls is made of soft gel. In some channels, as in figure 1, a provision is made for a pressure port ~ 2 mm upstream of the start of the test section. (The pressure port could not be fabricated exactly at the start of the test section, because there is leakage due to the deformation of the soft wall discussed below.) Since the outlet of the test section is open to atmosphere in the split inlet, the pressure measurement at the pressure port can be used to measure the pressure difference across the test section. We also fabricate micro-channels without the pressure port, in order to examine whether the pressure port has any effect on the flow dynamics. As in our earlier experiments on the flow through a tube (Verma & Kumaran 2012), there was no discernible difference between the mixing characteristics with and without the pressure port in any of the experiments reported here.

2.3. Experimental set-up

The set-up for conducting the experiments (figure 2) consists of two syringe pumps connected to the two inlets of the micro-channel mounted on a glass plate which is placed with flow axis along the x direction, the y coordinate along the height h_0 (100 and 160 μm) and z coordinate along the 1.5 mm width. The pressure port is connected to a pressure transducer (Druck model PDCR 810), which is connected to a computer to obtain pressure readings. The mixing of the dye-stream in the channel is monitored by a microscope and camera (A) with optical axis along the height (y -axis) of the

channel, as shown in figure 2. The camera B with optical axis along the z direction (spanwise direction) is used for monitoring the deformation of the channel. The two inlets of the micro-channel are connected to two syringe pumps C and D, through which fluid is pumped at the desired rates.

In the experiments with the Y inlet and Y outlet channel, there are surge tanks at the outlet within which conductance measurements are made, as shown in figure 2. In the experiments with the split inlet channel, the outlet is open to the atmosphere, and there are no additional attachments at the outlet. The laser shown in figure 2 is for detecting wall oscillations in the experiments with the split inlet, as discussed in § 2.5.

The pressure gradient across the soft section causes a deformation of the soft wall which varies with downstream position. The change in cross-sectional area with streamwise position along the channel results in a change in the flow velocity, since the flow rate is a constant. This also results in a change in the local Reynolds number based on the local velocity and height, as discussed in the next section on analytical methods. For clarity of representation, we use a single Reynolds number based on the flow rate and the width of the channel in our discussion,

$$Re = \frac{\rho Q}{W\eta} \quad (2.1)$$

where Q is the flow rate, W is the width of the channel in the z direction (~ 1.5 mm) and not the small dimension h_0 in the y direction. For an undeformed channel, the definition (2.1) is equal to $(\rho v_{av} h_0 / \eta)$, where v_{av} is the average velocity and h_0 is the height in figure 7(a). The shear modulus of the soft wall is expressed in terms of a dimensionless parameter Σ which is independent of the flow velocity,

$$\Sigma = \frac{\rho G' h_0^2}{\eta^2}. \quad (2.2)$$

2.4. Wall deformation

The application of a pressure drop across the test section also results in a deformation of the flexible wall, as shown in figure 3. This deformation is monitored by a microscope and camera (B) whose optical axis is aligned with the width (z -axis) of the channel, as shown in figure 2. The side view (in the x - y plane in figure 2) is shown in figure 3(a) for the undeformed channel. The image of the channel deformed due to the pressure gradient is shown in figure 3(b) for a gel with shear modulus 18 kPa and at a Reynolds number of 200 for the split inlet geometry. The superposed outline shows the deformation of the flexible wall. It should be noted that the deformation is not uniform across the width (z -axis) of the channel. The bottom soft wall is rigidly bonded to two sidewalls in the spanwise direction made of hard gel, and there is no deformation at these sidewalls. Therefore, the outline shown in figure 3(b) shows the maximum deformation at the mid-plane of the channel perpendicular to the z -axis. Wall deformation was measured for the split-inlet micro-channel, so that the flow modification due to deformation can be compared with CFD calculations in § 5.

2.5. Detection of wall oscillations

In order to detect motion in the wall, fluorescent microbeads of diameter 150 μm are incorporated into the soft wall as follows. When the film for the soft wall is cast, we first prepare a prepolymer layer of thickness 1.5 mm, and partially cure it for 10 minutes. The microbeads are gently spread on this layer. After this, an additional polymer layer of thickness of 0.5 mm is spread on top of the polymer film. The film

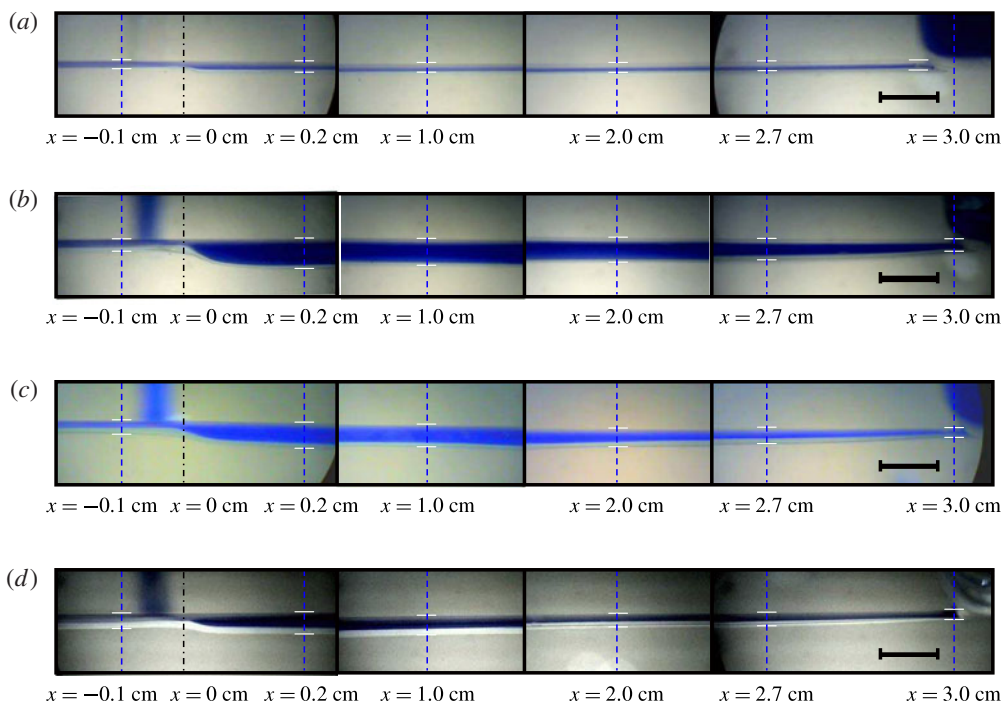


FIGURE 3. (Colour online) Side view of the (a) undeformed channel with no flow, (b) deformed channel with soft wall made using 1.75 % catalyst concentration and shear modulus 18 kPa, (c) 2.00 % catalyst concentration and shear modulus 25 kPa, and (d) 2.25 % catalyst concentration and shear modulus 35 kPa all at $Re = 222$. The Reynolds number is defined based on the flow rate in (2.1). The scale bar shown in the right of images is 1 mm. The locations where the height is measured are shown by the horizontal white lines, and the location $x = 0$ corresponds to the joint between the hard and soft sections.

of thickness 2 mm is then cured, with the embedded fluorescent microbeads. Owing to the high viscosity of the prepolymer and the small size of the beads, there is virtually no settling of the beads. The beads are illuminated by using a He–Ne laser of power 10 mW (model number OEM5R, Aerotech Inc.). The laser beam of thickness ~ 1 mm is directed along the x – y plane at an angle of $\sim 30^\circ$ to the horizontal, as shown in figure 2. Most of the laser beam passes through the channel, since the PDMS is transparent. However, there is scattering off the microbeads embedded in the PDMS wall, and the light scattered from the microbeads is captured by camera A above the channel. Owing to the low light intensity scattered from the microbeads, it is necessary to use a much lower resolution and a lower framing rate while taking images of the beads, in order to increase the light intensity incident on each pixel. Fluctuations in the intensity of the laser reflections are used to detect wall oscillations as follows (Verma & Kumaran 2012).

From the camera images, the intensity of the scattered light at each pixel is recorded for each frame. This is stored as a rectangular array of dimension $1 \leq i \leq 100$ and $1 \leq j \leq 50$ for image arrays of size 100×50 used here. If I_{ijk} is the greyscale value of the (i, j) pixel in frame k , the time-averaged intensity at each pixel, I_{ij}^{av} , is then

defined as

$$I_{ij}^{av} = \frac{1}{K} \sum_{k=1}^K I_{ijk}, \quad (2.3)$$

where the summation is carried out over all the frames 1 to K . The fluctuation in the intensity at pixel (i, j) and frame k is

$$\Delta I_{ijk} = I_{ijk} - I_{ij}^{av}. \quad (2.4)$$

The normalized mean square of the intensity fluctuations, F_I , is calculated as

$$F_I = \frac{\sum_{i,j} \left((1/K) \sum_{k=1}^K \Delta I_{ijk}^2 \right)}{\sum_{i,j} (I_{ij}^{av})^2}. \quad (2.5)$$

It should be noted that while the actual intensity recorded in individual experiments shows large variations, due to the varying number and size of beads in the field of view, the normalized mean square of the intensity fluctuations shows relatively little fluctuations, as shown by the error bars plotted with the results.

2.6. Segregation index from image analysis

The segregation index is determined from image analysis of the four fixed rectangular regions at four locations along the channel shown in figure 1(a) for the Y inlet channel. The images used for the image analysis, recorded using camera A in figure 2, are shown later in figure 12. The greyscale intensity of each pixel, B_{ij} , is determined, where i and j represent the indices of the pixels in the x and z directions, respectively. The average greyscale value across the entire channel, B^{av} , is

$$B^{av} = \frac{1}{N} \sum_{i,j} B_{ij}, \quad (2.6)$$

where N is the total number of pixels used for the averaging. The variance of the distribution is given by

$$\bar{B}^2 = \frac{1}{N} \sum_{i,j} (B_{ij} - B^{av})^2. \quad (2.7)$$

The segregation measure based on image analysis, S_I , is given by

$$S_I = \frac{\sqrt{\bar{B}^2}}{\Delta B}, \quad (2.8)$$

where ΔB is the difference between the pixel intensities of the light and dark regions in the laminar flow. For a well-mixed fluid, the intensity is uniform across the entire image, \bar{B}^2 is zero, and the segregation index S_I is equal to zero. When there is imperfect mixing of the two streams, \bar{B}^2 is greater than zero, and the segregation index has a maximum of 0.5 for no mixing between the two streams. Similar measures have been used earlier (Lee, Choi & Park 2010), where they are sometimes referred to as mixing index or degree of mixing. We prefer to use the term segregation index since the index is large when there is complete segregation, and zero when there is complete mixing.

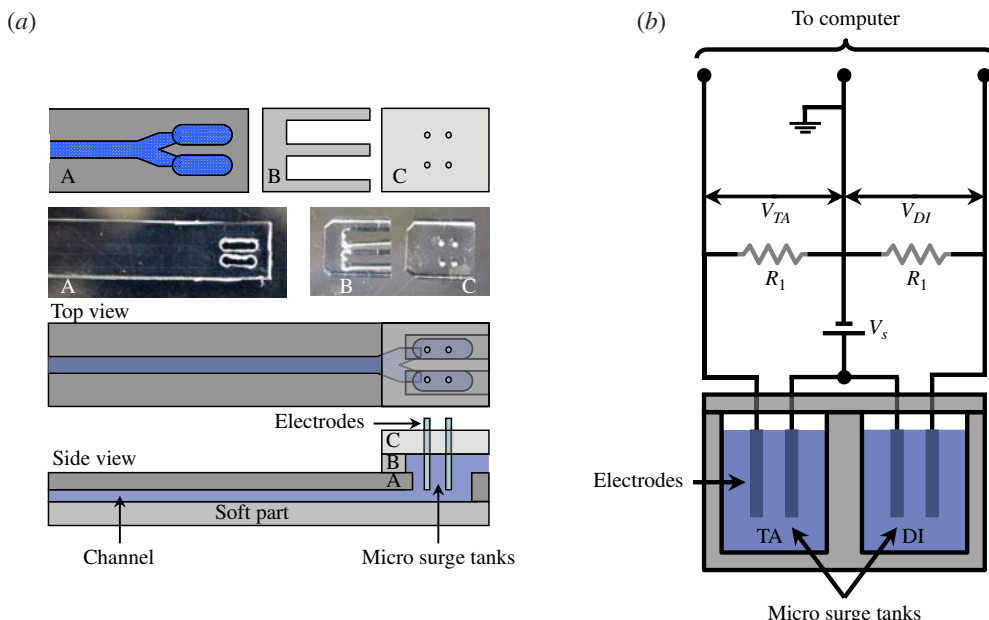


FIGURE 4. (Colour online) Micro surge tanks (a) for measuring conductivity, and the circuit used for the resistance probe (b). In (a), the schematic (top) and actual image (second from top) of the outlet of the channel with elliptical openings (A), the surge tank walls (B) and surge tank top with holes for electrodes (C); and schematics of the top view (third from top) and side view (bottom) of the surge tanks.

2.7. Mixing index from outlet concentration

In order to measure the mixing index based on concentration measurements, the Y outlet for the Y channel shown in figure 1(a) is used. At the outlet, two micro surge tanks are fabricated, and a pair of electrodes are inserted into each of the surge tanks, as shown in figure 2. The surge tanks are assembled on top of elliptical openings at the two outlets, as shown in figure 4(a). The size of the surge tanks, length ~ 4 mm, height ~ 2 mm and width ~ 2 mm, is such that the pressure drop due to these is small, while the volume of fluid is large enough so that the conductivity can be measured by the electrodes. It is important to ensure that the fluid height in the surge tanks does not change as the flow velocity is increased, since this could affect the conductance path between the electrodes and consequently the resistance measurements.

Each resistance probe consists of two copper wires separated by a distance of 2 mm along the length of each outlet, across which the resistance is measured as follows. The probe is connected in series to a resistor of known resistance, $R_1 = 500 \text{ k}\Omega$, and connected to a power source with voltage V_s , as shown in figure 4(b). In all of our measurements, a 12 V DC power supply was used as the power source, and the same DC power supply was used for both resistance probes, to ensure that the voltages are the same. The voltage across the known resistors, V_{TA} and V_{DI} , were measured through the I/O data card (National Instruments NI USB-6009) of the computer.

Before carrying out the concentration measurements, the relationship between the concentration and the voltages V_{TA} and V_{DI} are obtained by calibration. For this, a well-mixed solution of known concentration c of tannic acid is injected through both syringe pumps C and D in figure 2. The voltage V_R (V_{TA} or V_{DI}) for the two electrodes

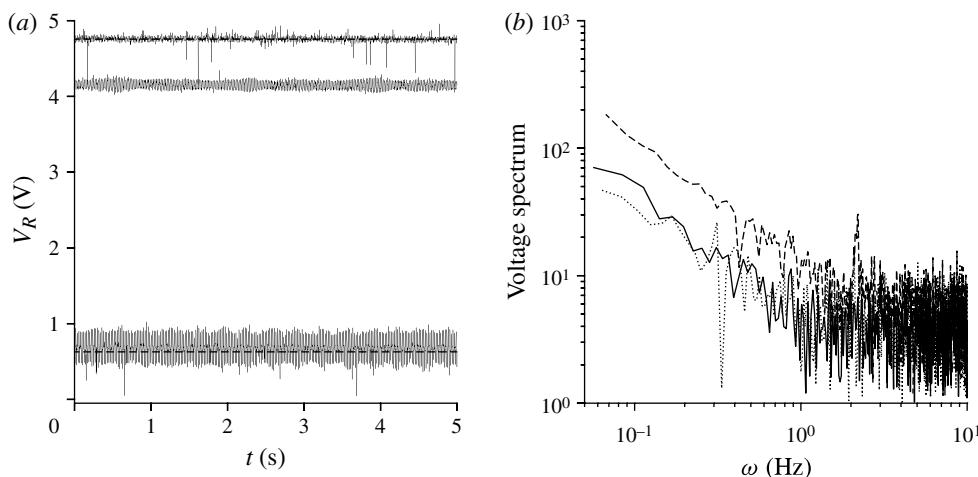


FIGURE 5. The measured voltage V_R as a function of time (a) and the spectrum of the measured voltage as a function of frequency in Hertz (b) for pure de-ionized water (lower curve in a, dotted line in b), tannic acid of concentration $2.5 \times 10^{-3} \text{ g ml}^{-1}$ (upper curve in a, dashed line in b) and tannic acid of concentration $1.25 \times 10^{-3} \text{ g ml}^{-1}$ (middle curve in a, solid line in b).

in figure 4(b) is measured independently, and the calibration curve is obtained for the voltage V_R as a function of the concentration. The raw voltage signal is fluctuating in time, as shown in figure 5(a). The average voltage, when compared with suitable calibration as discussed below, gives the average value of the tannic acid concentration. However, we can obtain further information by taking the power spectrum of the voltage as shown in figure 5(b). In our frequency spectra, there is a dominant peak at $\sim 50 \text{ Hz}$, along with higher harmonics, due to the frequency of the input AC power. We focus attention on frequencies less than 10 Hz , where this peak is not observed, and where there is no distortion due to the background frequency. The power spectra of the voltage signals give the frequencies of the concentration fluctuations at the outlet, and when compared with the spectra for premixed tannic acid solutions of equal concentration injected in both inlets, serves as an indicator of the quality of mixing in the channel.

This calibration is carried out prior to each experiment for the variation of concentration with Reynolds number, and each experiment is carried out three times in order to obtain the error bars. This is because there is a variation in the mean value of the voltage for the same concentration in different experiments, due to the sensitivity of the voltage to small variations in separation between electrodes and to micro surge tank dimensions. This variation is shown for three different gel samples with the same wall shear modulus in figure 6(a). Although the difference in voltage between different samples is small, it is important to calibrate independently for each sample, since there are relatively large errors due to the small variations in the concentration if an average calibration curve is used. For a given sample, there is virtually no variation in the voltage V_R with Reynolds number or flow velocity, as shown in figure 6(b). This indicates that convective effects are not a factor in determining the conductivity of the solution, and the voltage is determined by the concentration alone.

In the mixing experiments, pure de-ionized (DI) water is injected into one inlet through pump C, and tannic acid solution of concentration $c_0 = 2.5 \times 10^{-3} \text{ g ml}^{-1}$ is

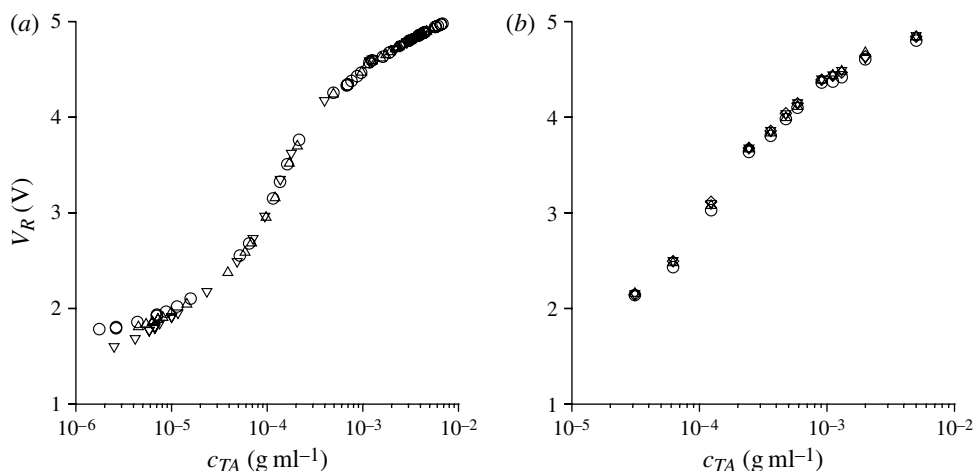


FIGURE 6. Average voltage V_R across one of the electrodes in figure 4(b) with tannic acid concentration c_{TA} for experiments on three different samples with shear modulus 35 kPa for the soft wall. The symbols in (a) show the results for three different independent samples to illustrate the sample-to-sample variation in the calibration curve, while the symbols in (b) show the results for one sample at different flow rates: \circ , $Re = 67$, $Q = 0.1 \text{ ml s}^{-1}$; \triangle , $Re = 111$, $Q = 0.17 \text{ ml s}^{-1}$; ∇ , $Re = 200$, $Q = 0.3 \text{ ml s}^{-1}$; \diamond , $Re = 244$, $Q = 0.37 \text{ ml s}^{-1}$.

injected into the other inlet through pump D. The concentration is measured using the resistance probe separately in the outlet on the same side as the DI water inlet (referred to as the DI water outlet) and in the outlet on the same side as the tannic acid inlet (referred to as the TA outlet). If there is no mixing, the DI water outlet will contain DI water with concentration 0, and the TA outlet will contain tannic acid with concentration c_0 . In the case of complete mixing, the concentration is $(c_0/2)$ in the two outlets. Figure 6 shows that there is a significant increase in the voltage (from ~ 2 to $\sim 4.2 \text{ V}$) when the tannic acid concentration increases from 10^{-4} to $1.25 \times 10^{-3} \text{ g cc}^{-1}$, but the variation is much less (from ~ 4.2 to $\sim 4.6 \text{ V}$) when the tannic acid concentration increases from 1.25×10^{-3} to $2.5 \times 10^{-3} \text{ g cc}^{-1}$. Owing to this, the variation in the voltage in the DI water outlet is much higher than that in the TA outlet, and the concentration in the former can be determined more accurately. Therefore, we determine the concentration in the DI water outlet from the voltage measurement, and infer that in the TA outlet from mass balance. On the basis of the outlet concentrations, the mixing index is defined as

$$M_I = \frac{c_{DI}}{c_0/2}, \quad (2.9)$$

where c_{DI} is the concentration in the DI water outlet. This mixing index will vary between 0 (for no mixing) and 1 (for complete mixing, where $c_{DI} = (c_0/2)$).

3. Analytical methods

3.1. Flow simulation

In order to make comparisons of the pressure drop across the channel with predictions from the numerical solutions of the Navier–Stokes equations, it is necessary to reconstruct the deformed shape of the channel. This reconstruction is carried out

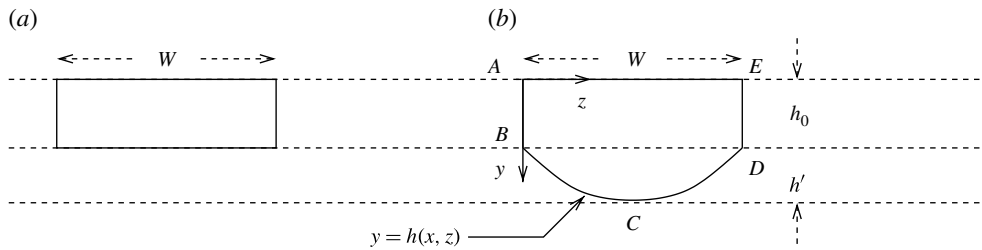


FIGURE 7. Undeformed (a) and deformed (b) cross-sections of the channel.

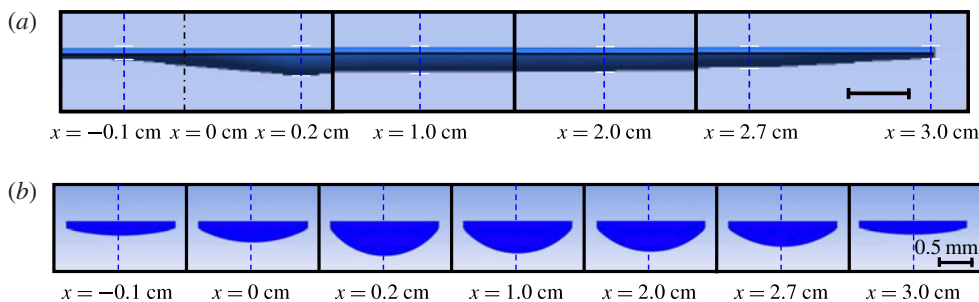


FIGURE 8. (Colour online) The side view (a) and the cross-sectional views at different locations (b) of the reconstructed shape of the channel shown in figure 3(c) in which the soft wall has shear modulus 25 kPa, and at Reynolds number 244. The scale bar in (a) is 1 mm and that in (b) is 0.5 mm.

as shown in figure 7. The undeformed cross-section of the channel has width $W = 1.5$ mm and height $h_0 = 100/160$ μm , as shown in figure 7(a). Owing to the deformation, the deformed shape shown in figure 7(b) has a maximum height $h_0 + h'$, which is obtained from the side view in figure 3. From this, the maximum deformation h' is calculated. The deformed bottom wall of the channel in figure 7(b) is obtained using a cubic fit, from the locations of the points B, C and D, and from the symmetry condition that the slope is zero at the point C of maximum deformation. The deformed shape $h(x, z)$ is calculated at each x location, and the deformed bottom wall of the channel is reconstructed for the numerical simulations.

The reconstructed deformed shape of the channel, obtained from the image in figure 3(c), is shown in figure 8. The side view, in figure 8(a), shows the deformation at the centre of the channel in the spanwise direction where there is maximum deformation, while the cross-sectional views in figure 8(b) are reconstructed using the cubic fit discussed in relation to figure 7.

The ANSYS FLUENT 13.0.0 CFD program was used to calculate the velocity field and the pressure drop in the deformed channel. The pressure–velocity formulation was used, and the fluid was modelled using a laminar flow model for a Newtonian fluid. The computational domain consisted of the entire channel of length 4 cm, including the hard and soft sections. Zero-velocity boundary conditions are specified on all solid surfaces for the base steady-state flow (although surface motion is taken into account in the linear stability analysis discussed in § 3.2). A constant velocity was specified at the inlet, and a constant pressure condition was specified at the outlet. The specific velocity profile at the entrance does affect the pressure variation and flow evolution

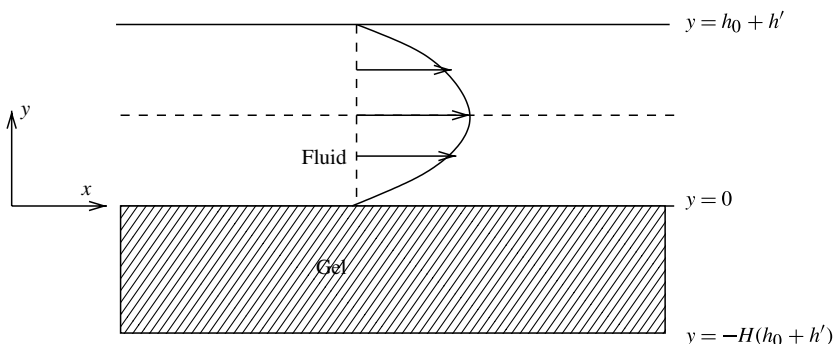


FIGURE 9. Schematic diagram showing the configuration and coordinate system for the linear stability analysis.

in the development section, but we found that there is little effect downstream in the test section between the pressure port and the outlet (see figure 1*b*) where the pressure drop is compared with experiments. The simulation was initialized with zero velocity everywhere, the system was allowed to evolve until steady state is reached and the convergence limit was set at 10^{-4} in the residual for the continuity equation (the limiting condition in most simulations) or 10^{-3} for the velocity equations.

The channel was discretized with a spatial resolution of $20\text{ }\mu\text{m}$, that is, the grid points in the simulations were separated by $20\text{ }\mu\text{m}$ in all three directions. For the deformed channel shape shown in figure 8, this required 9.1×10^5 nodes. We have also carried out simulations with coarser and finer discretization where the separation was $30\text{ }\mu\text{m}$ (2.7×10^5 grid points) and $15\text{ }\mu\text{m}$ (2.1×10^6 grid points), to check grid independence. The grid independence is verified in figure 20 for the simulation of the experimental configurations, and the simulation procedure is validated for a channel with rectangular cross-section in appendix B.

3.2. Linear stability analysis

The system consists of a pressure-driven flow of an incompressible Newtonian fluid of density ρ and viscosity η in a rectangular channel with an elastic solid layer at the bottom and a rigid surface on top, as shown in figure 9. A Cartesian coordinate system is used, where the flow is in the x direction and the velocity gradient is in the y direction. We consider a fluid layer of thickness $(h_0 + h')$ equal to the maximum height of the deformed channel (since we are performing the linear stability analysis along the centreline in the spanwise direction) occupying the domain $0 < y < h_0 + h'$. The fluid layer is bounded by a rigid surface at $y = h_0 + h'$, and the fluid–solid interface at $y = 0$. The thickness of the solid layer is defined as $H(h_0 + h')$, where H , the ratio of the two thicknesses, is determined from the experiments. The viscoelastic solid layer in the region $-H(h_0 + h') \leq y \leq 0$ is bounded by a rigid surface $y = -H(h_0 + h')$, and the fluid–solid interface at $y = 0$. The deformable solid layer is modelled as an incompressible viscoelastic neo-Hookean solid of density ρ and shear modulus G' .

For simplicity, we assume that the densities of the solid and fluid are equal. The relative density of the soft polydimethyl siloxane gels synthesized for the experiments, using cross-linker concentrations lower than those specified by the manufacturer, was in the range 1.03–1.06; this is lower than the manufacturer-specified value of 1.12 for the standard gel formulation. Owing to this small difference in densities, it is a good approximation to assume that densities are equal. Surface tension at the liquid–solid

interface is neglected because it is small in the experimental system. A dimensionless ratio of surface tension and elastic stresses is $(T/((h_0 + h')G'))$, where T is the surface tension. For a gel which shear modulus of order 10^4 Pa, surface tension 10^{-2} N m $^{-1}$ and $h_0 + h' \sim 100$ μ m, the ratio $(T/((h_0 + h')G'))$ is $\sim 10^{-2}$. For simplicity, we also neglect dissipation in the solid. Solid dissipation does have a significant effect on the flow stability in the low-Reynolds-number limit, but previous studies have shown that there is very little effect for Reynolds numbers greater than ~ 100 . The base flow configuration and the coordinate system are shown in figure 9.

The method of analysis is identical to that of Gaurav & Shankar (2010), with two important differences. First, we have a rigid wall at the boundary at $y = h_0 + h'$, in contrast to Gaurav & Shankar (2010) who had a flexible surface. Secondly, we do not consider a parabolic flow, as was done by Gaurav and Shankar, but we derive equations for a general flow profile and pressure variation, assuming only that the velocity profile is locally parallel. Owing to this, the base state solutions and the linear stability equations are briefly provided for the present case. Our equations are restricted to the simple case where there is no solid dissipation, in order to obtain the lower bound for the transition Reynolds number. The extension to include solid dissipation is discussed by Gaurav & Shankar (2010).

In the linear stability analysis, we first scale all variables from this point onwards, so that all equations are non-dimensional in the following analysis and the results. The appropriate length scale is the maximum height of the deformed channel $(h_0 + h')$, the cross-stream coordinate is defined as $y^* = (y/(h_0 + h'))$, the stress is scaled by the shear modulus G' , $\sigma_{ij}^* = \sigma_{ij}/G'$, time is scaled by the ratio of the viscosity and elasticity (η/G') , $t^* = (tG'/\eta)$, the displacement within the solid is scaled by $(h_0 + h')$, $w_i^* = w_i/(h_0 + h')$, and all velocities are scaled by $((h_0 + h')G'/\eta)$, $v_i^* = (v_i\eta/G'(h_0 + h'))$. After scaling, as shown below there are only two dimensionless group in the scaled equations, the parameter $\Sigma' = (\rho G(h_0 + h')^2/\eta^2)$ and a scaled mean velocity. The superscript $*$ is omitted in the following analysis for simplicity, but while discussing the numerical results later (§ 5), the non-dimensionalization is stated explicitly.

The mass and momentum conservation equations for the fluid are the usual incompressible Navier–Stokes equations,

$$\nabla \cdot \mathbf{v} = 0 \quad (3.1)$$

$$\Sigma' \left(\frac{\partial \mathbf{v}}{\partial t} + \mathbf{v} \cdot \nabla \mathbf{v} \right) = -\nabla p + \nabla^2 \mathbf{v}, \quad (3.2)$$

where the dimensionless parameter $\Sigma' = (\rho G(h_0 + h')^2/\eta^2)$, appears due to the non-dimensionalization. We use a parallel flow approximation for the base state, where the velocity \bar{v}_x is only a function of the y coordinate.

The displacement field \mathbf{w} is the dynamical variable describing the solid deformation. We use an Eulerian description, where the displacement field is defined in terms of the unstressed coordinates,

$$\mathbf{w}(\mathbf{X}, t) = \mathbf{x}(\mathbf{X}, t), \quad (3.3)$$

where \mathbf{x} is the location of a material point whose unstressed position is \mathbf{X} . The deformation tensor \mathbf{F} is defined as

$$\mathbf{F} = \nabla_{\mathbf{X}} \mathbf{w}. \quad (3.4)$$

The Cauchy stress tensor, when scaled by the shear modulus G' , is given by

$$\boldsymbol{\sigma} = -p_s \mathbf{I} + \mathbf{F} \cdot \mathbf{F}^T, \quad (3.5)$$

where p_s is the pressure in the solid. For an incompressible solid where the volume is conserved, the determinant of the deformation tensor is 1,

$$\text{Det}(\mathbf{F}) = 1. \quad (3.6)$$

The momentum conservation equation just states that the rate of change of velocity in the material is equal to the divergence of the stress,

$$\Sigma' \left(\frac{\partial^2 \mathbf{w}}{\partial t^2} \right) = \nabla_X \cdot \mathbf{P}, \quad (3.7)$$

where \mathbf{P} is Piola–Kirchoff stress tensor defined in indicial notation as

$$P_{IJ} = F_{IK}^{-1} \sigma_{KJ}^e, \quad (3.8)$$

where σ_{IJ}^e is the Cauchy stress tensor. Here, we use lowercase subscripts in the indicial notation for the fluid and uppercase superscripts for the solid to distinguish the two. Inserting the Piola–Kirchoff stress tensor into the momentum conservation equation (3.7), we find

$$\Sigma' \frac{\partial^2 w_I}{\partial t^2} = \frac{\partial (p F_{JI}^{-1})}{\partial X_J} + \frac{\partial F_{IJ}}{\partial X_J}. \quad (3.9)$$

In the base state, a unidirectional flow in the x direction is considered, where the velocity profile is \bar{v}_x is a function of y and $\bar{v}_y = 0$. We do not use the quadratic profile for a fully developed parabolic flow which satisfies the no-slip condition at $y = 0$ and $y = 1$,

$$\bar{v}_x = -\frac{\partial p}{\partial x} \left(\frac{y}{2} - \frac{y^2}{2} \right) \quad (3.10)$$

but adopt the velocity profile from the CFD simulations at different streamwise locations. The fluid–solid interface is flat in the base state with a non-zero displacement in x direction due to shear stress exerted by fluid at this interface $y = 0$. The boundary conditions for the fluid at the fluid–solid interface become $v_x = 0$ and $v_y = 0$, and the normal and tangential stress balance conditions are $\tau_{yy} = \sigma_{YY}$, $\tau_{xy} = \sigma_{XY}$, respectively, where τ_{ij} is the stress in the fluid given by Newton’s law of viscosity, and σ_{IJ} is the stress in the solid wall. The boundary conditions for deformable solid wall at $y = -H$ is $\mathbf{w} = \mathbf{X}$ because there is no deformation at the rigid surface.

The deformation field in the solid layer is obtained by solving the governing mass and momentum equations (3.6) and (3.7). From equation (3.6), we find

$$\frac{\partial \bar{w}_X}{\partial X} \frac{\partial \bar{w}_Y}{\partial Y} - \frac{\partial \bar{w}_Y}{\partial X} \frac{\partial \bar{w}_X}{\partial Y} = 1. \quad (3.11)$$

where the overbars denote variables in the base state. The momentum conservation equations reduce to

$$-\frac{\partial \bar{p}_s}{\partial X} + \frac{\partial^2 \bar{w}_X}{\partial Y^2} = 0, \quad (3.12)$$

$$-\frac{\partial \bar{p}_s}{\partial Y} + \frac{\partial \bar{p}_s}{\partial X} \frac{\partial \bar{w}_X}{\partial Y} = 0, \quad (3.13)$$

with zero displacement conditions at the boundary where the scaled $y = -H$,

$$\bar{w}_X - X = \bar{w}_Y - Y = 0, \quad (3.14)$$

and stress boundary conditions at the surface $Y = 0$,

$$\bar{\sigma}_{YY} = -\bar{p}_s + 1 = -\bar{p}, \quad (3.15)$$

$$\bar{\sigma}_{XY} = \frac{\partial \bar{w}_X}{\partial y} = \dot{\gamma}_w, \quad (3.16)$$

where $\dot{\gamma}_w$, the strain rate at the wall, is

$$\dot{\gamma}_w = \left. \frac{\partial \bar{v}_x}{\partial y} \right|_{y=0}. \quad (3.17)$$

Equations (3.12) and (3.13) can be solved to obtain the displacement field,

$$\bar{w}_X = X - \frac{1}{2} \frac{\partial \bar{p}}{\partial X} (H^2 - Y^2) + \dot{\gamma}_w (H + Y), \quad (3.18)$$

$$\bar{p}_s = \bar{p} + \left(\frac{\partial \bar{p}}{\partial x} \right)^2 \frac{Y^2}{2} + \frac{\partial p}{\partial x} \dot{\gamma}_w Y + 1. \quad (3.19)$$

where \bar{p} , the pressure in the fluid, depends only on the downstream position x .

In the linear stability analysis, small perturbations are imposed on the velocity and wall displacement fields of the form,

$$v_i = \bar{v}_i + \tilde{v}_i(y) \exp(\iota k(x - ct)), \quad (3.20)$$

$$w_i = \bar{w}_i + \tilde{w}_i(Y) \exp(\iota k(X - ct)), \quad (3.21)$$

where k is the wavenumber and c is the wave speed. The wavenumber is real and wave speed is complex for the temporal stability analysis, while the frequency is real and wavenumber complex for the spatial stability analysis. The Fourier expansions in (3.20) and (3.21) are valid only in the parallel flow approximation where the streamlines are parallel, and when the variation of the mean velocity with streamwise location is neglected. This requires that the wavelength of the most unstable modes is smaller than the length scale for the flow development, and the length scale for variation in the spanwise direction. We examine these assumptions once again while discussing the numerical results (§ 5). At this point, we derive the linear stability equations for the general case with complex k and c .

Equations (3.20) and (3.21) are inserted into the fluid conservation equations, and linearized to obtain the mass conservation equation and the combined Orr–Sommerfeld equation for the momenta in the x and y directions,

$$d_y \tilde{v}_y + \iota k \tilde{v}_x = 0, \quad (3.22)$$

$$\Sigma' \iota k (\bar{v}_x - c) \tilde{v}_y + = -d_y \tilde{p} + (d_y^2 - k^2) \tilde{v}_y, \quad (3.23)$$

$$\Sigma' (\iota k (\bar{v}_x - c) \tilde{v}_x + \tilde{v}_y d_y \bar{v}_x) = -\iota k \tilde{p} + (d_y^2 - k^2) \tilde{v}_x. \quad (3.24)$$

where $d_y \equiv (d/dy)$. The pressure can be eliminated by adding $\iota k \times$ (3.23) and $(-d_y)$ times (3.24). After expressing $\tilde{v}_x = -(d_y \tilde{v}_y / \iota k)$ from the mass conservation equation, we obtain

$$\Sigma' (\iota k (\bar{v}_x - c) (d_y^2 - k^2) \tilde{v}_y - \tilde{v}_y d_y^2 \bar{v}_x) = (d_y^2 - k^2) (d_y^2 - k^2) \tilde{v}_y. \quad (3.25)$$

The incompressibility condition for the wall material, $\text{Det}(\mathbf{F}) = 1$, reduces to

$$\iota k \tilde{w}_X + d_Y \tilde{w}_Y - \frac{\partial \bar{w}_X}{\partial Y} \iota k \tilde{w}_Y = 0. \quad (3.26)$$

The momentum conservation equations for the wall material are

$$-\Sigma' k^2 c^2 \tilde{w}_x = -\iota k \tilde{p}_s - \frac{\partial \tilde{p}_s}{\partial X} d_Y \tilde{w}_Y + \frac{\partial \tilde{p}_s}{\partial Y} \iota k \tilde{w}_Y + (d_Y^2 - k^2) \tilde{w}_x, \quad (3.27)$$

$$-\Sigma' k^2 c^2 \tilde{w}_Y = -d_Y \tilde{p}_s - \iota k \tilde{w}_X \frac{\partial \tilde{p}_s}{\partial Y} + \frac{\partial \tilde{p}_s}{\partial X} d_Y \tilde{w}_X + \iota k \tilde{p}_s \frac{\partial \tilde{u}_X}{\partial Y} + (d_Y^2 - k^2) \tilde{w}_Y. \quad (3.28)$$

Using the equations for the mean displacement and pressure fields (3.18) and (3.19), the above equations reduce to

$$\iota k \tilde{w}_X + d_Y \tilde{w}_Y - \iota k \tilde{w}_Y \left(\dot{\gamma}_w + Y \frac{\partial \bar{p}}{\partial x} \right) = 0, \quad (3.29)$$

$$-k^2 c^2 \tilde{w}_x = -\iota k \tilde{p}_s - \frac{\partial \bar{p}}{\partial x} d_Y \tilde{w}_Y + \left(\dot{\gamma}_w + \frac{\partial \bar{p}}{\partial x} Y \right) \iota k \tilde{w}_Y + (d_Y^2 - k^2) \tilde{w}_x, \quad (3.30)$$

$$\begin{aligned} -k^2 c^2 \tilde{w}_Y = & -d_Y \tilde{p}_s - \iota k \tilde{w}_X \left(\dot{\gamma}_w + \frac{\partial \bar{p}}{\partial x} Y \right) + \frac{\partial \bar{p}}{\partial x} d_Y \tilde{w}_X + \iota k \tilde{p}_s \left(\frac{\partial \bar{p}}{\partial x} Y + \dot{\gamma}_w \right) \\ & + (d_Y^2 - k^2) \tilde{w}_Y. \end{aligned} \quad (3.31)$$

The boundary conditions at $y = 1$ are the no-slip conditions, $\tilde{v}_x = \tilde{v}_y = 0$, while the boundary conditions at $Y = -H$ are the zero displacement conditions, $\tilde{w}_x = \tilde{w}_Y = 0$. (It is important to note that all lengths have been scaled by $(h_0 + h')$ in the analysis). At the perturbed interface $Y = \tilde{w}_Y$, the velocity and stress continuity conditions are used. When the interfacial conditions are written in terms of the fields at the unperturbed interface $Y = 0$ using an expansion in \tilde{w}_Y , we obtain,

$$\tilde{v}_y = -\iota k c \tilde{w}_Y, \quad (3.32)$$

$$\tilde{v}_x + \dot{\gamma}_w \tilde{w}_Y = -\iota k c \tilde{w}_X. \quad (3.33)$$

In the above equation, the second term on the left accounts for the variation in the mean velocity in the fluid due to the displacement of the surface. For the mean velocity gradient at the wall, $\dot{\gamma}_w$, given in (3.17), and the mean displacement fields given in (3.18) and (3.19), the stress balance equations at the interface are

$$-\tilde{p}_f + 2d_Y \tilde{v}_y = -\tilde{p}_s + 2d_Y \tilde{w}_Y, \quad (3.34)$$

$$d_Y \tilde{v}_x + \iota k \tilde{v}_y = d_Y \tilde{w}_X + \iota k \tilde{w}_Y + d_Y \tilde{w}_Y \dot{\gamma}_w - \iota k \tilde{w}_Y \dot{\gamma}_w^2. \quad (3.35)$$

The incompressibility conditions (3.22) and (3.29) can be used to express \tilde{v}_x and \tilde{w}_X in terms of \tilde{v}_y and \tilde{w}_Y in the (3.35), to obtain

$$-(\iota k)^{-1} d_Y^2 \tilde{v}_y + \iota k \tilde{v}_y = -(\iota k)^{-1} d_Y^2 \tilde{w}_Y + \iota k \tilde{w}_Y + 2d_Y \tilde{w}_Y \dot{\gamma}_w - \iota k \tilde{w}_Y \dot{\gamma}_w^2. \quad (3.36)$$

The solution procedure is as follows. The equations for the displacement field, equations (3.29), (3.30) and (3.31) can be reduced to one equation for the displacement \tilde{w}_Y . This resulting displacement equation, along with (3.25) for the velocity field, are framed as a composite set of equations, along with the boundary conditions $\tilde{v}_x = \tilde{v}_y = 0$ at $y = 1$ (top rigid surface), $\tilde{w}_x = \tilde{w}_Y = 0$ at $Y = -H$ (bottom rigid surface bounding the gel) and the matching conditions at the interface, (3.32), (3.33), (3.34) and (3.36). Once the solutions to these equations are obtained, the pressure fields are obtained from (3.24) and (3.30).

The composite system of equations and boundary conditions is solved using the pseudo-spectral collocation method (Boyd 1989; Weideman & Reddy 2000). The unknown velocity and displacement fields are expressed as the sum of N Chebyshev polynomials each, and these are substituted into the governing equations and set to

zero at $(N - 4)$ Gauss–Lobatto collocation points each in the fluid and the solid, to obtain a set of $(2N - 8)$ equations. The remaining eight equations are obtained from the boundary conditions, two for the fluid $\tilde{v}_x = \tilde{v}_y = 0$ at $y = 1$, two for the solid $\tilde{w}_x = \tilde{w}_y = 0$ at $y = -H$, and four matching conditions (3.32), (3.33), (3.34) and (3.36) at the interface. This provides a $2N \times 2N$ matrix, which can be solved to obtain the wave speed c for specified Σ' , flow velocity and wavenumber k . This matrix eigenvalue problem is solved using the *polyeig* function in MATLAB, to given $2N$ eigenvalues. The spurious eigenvalues are filtered out by increasing the number of modes N , and checking for convergence. We used a two values of $N = 50$ and $N = 60$ to get the convergent results discussed in § 5. The linear stability calculations were first validated with the results of Gaurav & Shankar (2010) for the parabolic flow in a channel with flat walls, and found quantitative agreement for the eigenvalues for that problem. The same eigenvalue search procedure was used for the velocity profiles predicted by the CFD simulations in our linear stability analysis.

The solution procedure provides the eigenvalues as a function of the wavenumber k for specified values of \tilde{v}_x , Σ' and the pressure gradients in the mean flow. The value of Σ' is fixed from the experimental results, and the wave speed c is calculated for increasing \tilde{v}_x (or Reynolds number). At the transition Reynolds number, the imaginary part of c passes through zero, indicating neutral modes. It should be noted that even though the linear stability equations apparently depend only on the parameter Σ' , there is also a dependence on the local Reynolds number $Re' = (\rho \tilde{v}_{av}(h_0 + h')/\eta)$ through the mean velocity and strain rate. In the non-dimensionalization scheme used here, the scaled mean velocity is defined as $\tilde{v}_x^* = (\tilde{v}_x \eta / G'(h_0 + h'))$. When expressed in terms of the velocity averaged over the profile \tilde{v}_{av} ,

$$\tilde{v}_{av} = (h_0 + h')^{-1} \int_0^{h_0+h'} dy v_x \quad (3.37)$$

the scaled velocity is $\tilde{v}_x^* = (\tilde{v}_x / \tilde{v}_{av})(\rho \tilde{v}_{av}(h_0 + h')/\eta)(\eta^2 / \rho G'(h_0 + h')^2) = (\tilde{v}_x / \tilde{v}_{av})(Re' / \Sigma')$. A similar non-dimensionalization can be carried out for the local wall strain rate $\dot{\gamma}_w$ which appears in the boundary conditions. For this reason, the results depend on both Re' and Σ' .

4. Experimental results

The change in cross-sectional area with streamwise position along the channel results in a variation in the flow velocity, since the flow rate is a constant. This also results in a change in the local Reynolds number based on the local velocity and height, as discussed in the following section. For clarity of representation, we use a single Reynolds number based on the flow rate and the width of the channel (2.1). For the soft wall, the shear modulus is expressed in terms of the dimensionless parameter Σ in (2.2). In our theoretical studies, we have the additional parameters Σ' defined after (3.2), and $Re' = (\rho \tilde{v}_{av}(h_0 + h')/\eta)$ based on the local $(h_0 + h')$ instead of h_0 , and \tilde{v}_{av} which is the average for the velocity profile along the central plane in the spanwise direction calculated using (3.37). This is because the relevant length scale for the linear stability analysis along the central plane of the channel in the streamwise direction is $(h_0 + h')$, and the relevant velocity is the average of the velocity profile in this plane. When the results of the linear analysis are finally compared with experiments, all results are expressed in terms of the parameters Re and Σ to avoid confusion.

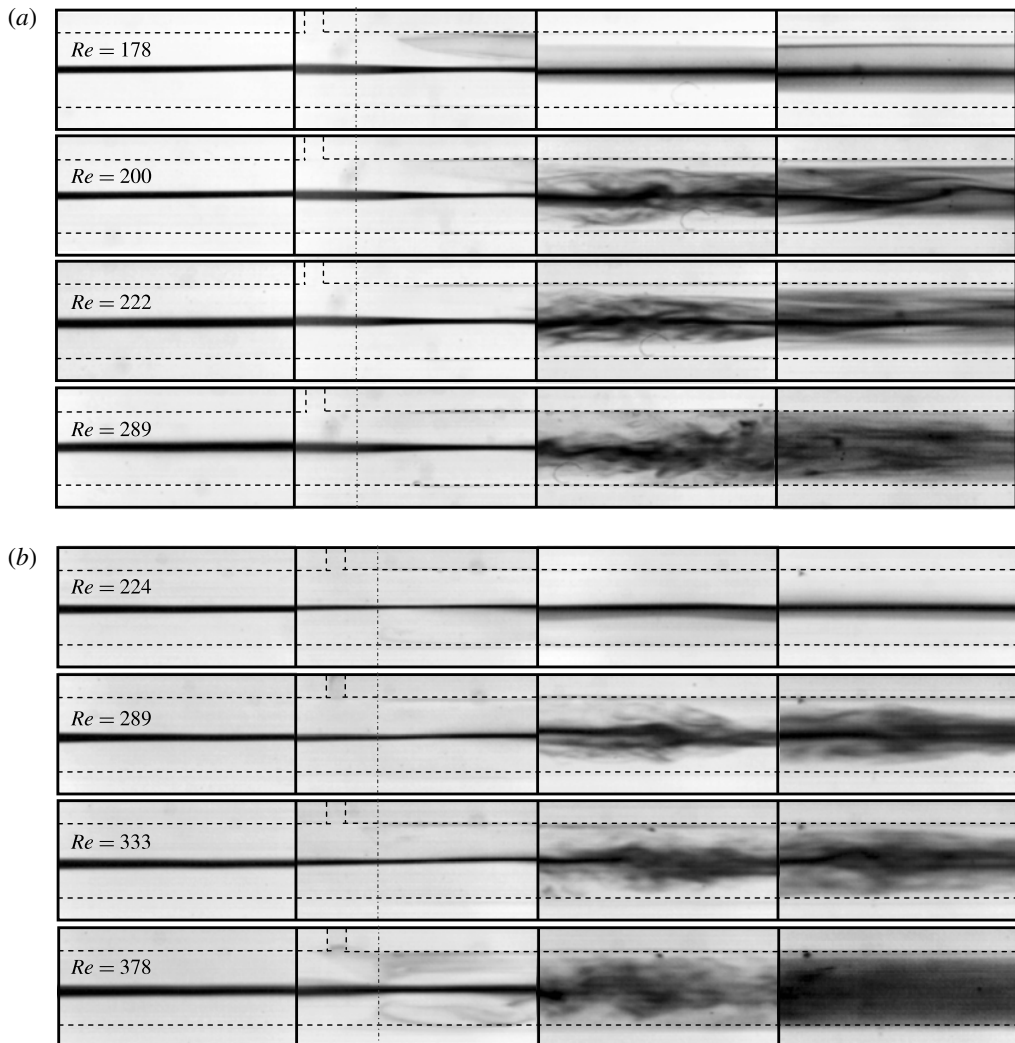


FIGURE 10. For caption see the next page.

All experiments in § 4.1 are carried out using the split inlet geometry in figure 1(b), while all experiments in § 4.2 are carried out using the Y inlet geometry in figure 1(a) so that the outlet stream can also be split into two.

4.1. Dye-stream experiments and wall oscillations

In the dye-stream experiments, coloured dye is pumped in through the central channel in figure 1(b), while clear water is pumped through the two outer channels. The images of the dye stream, captured using the camera A in figure 2, are shown in figure 10 for soft walls with different shear moduli for a channel whose height is $100\ \mu\text{m}$ in the absence of flow. The four images, from left to right, in figure 10 are centred at locations 0.5 cm upstream, 0.1 cm downstream, 1 cm downstream and 2 cm downstream of the entrance to the test section.

For the soft wall with shear modulus 18 kPa and $\Sigma = 1.75 \times 10^5$, we observe dye-stream oscillations at a Reynolds number of 178, but the dye-stream breaks up at

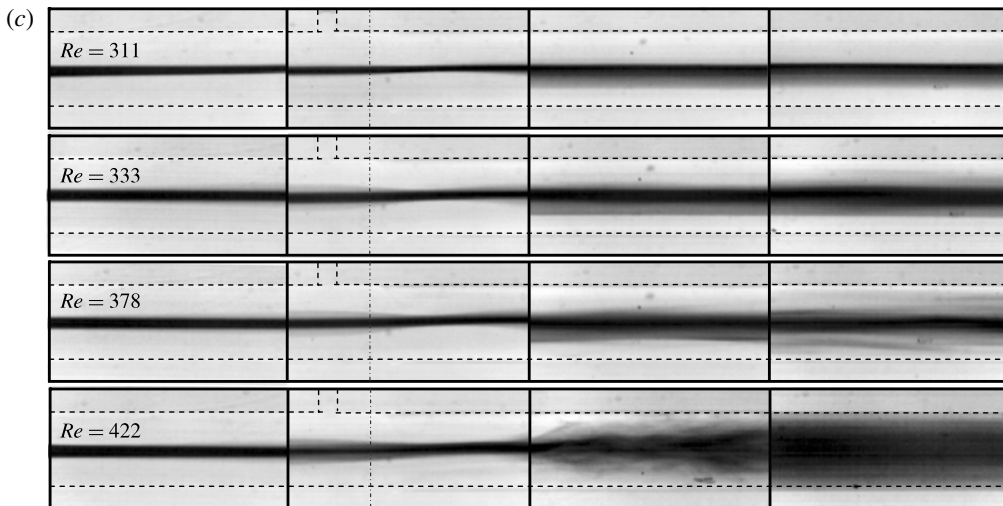


FIGURE 10. (contd). Images of the dye-stream experiments for a channel of height $100\text{ }\mu\text{m}$ with soft wall prepared using shear modulus 18 kPa and $\Sigma = 1.75 \times 10^5$ (a), shear modulus 25 kPa and $\Sigma = 2.51 \times 10^5$ (b) and shear modulus 35 kPa and $\Sigma = 3.80 \times 10^5$ (c). The horizontal dashed lines show the channel boundaries, the vertical dot-dashed line in the second image from left shows the junction between the hard and soft sections and the outlet at the top in the second image from the left shows the location of the pressure port. The images are centred at 0.5 cm upstream, 1 mm downstream, 1 cm downstream and 2 cm downstream of the junction between the hard and soft sections. The reference length is provided by the 1.5 mm width of the channel.

a Reynolds number of 200. For soft wall with gel with shear modulus 25 kPa and $\Sigma = 2.51 \times 10^5$, there are perceptible oscillations in the dye stream for a Reynolds number of 244 and the dye stream ruptures at a Reynolds number of 289. In the case of the soft wall with shear modulus 35 kPa and $\Sigma = 3.80 \times 10^5$, perceptible oscillations in the dye stream are observed at a Reynolds number of 311, although dye breakup is observed at a Reynolds number of 422. An important observation is that the instability is first observed not at the expanding section 0.1 cm downstream of the entrance to the test section (see figure 3), but rather in the contracting downstream section $>2.0\text{ cm}$ downstream of the entrance to the test section. Thus, the flow first becomes unstable in the downstream contracting section where the deformation is relatively small, and not at the upstream expanding section which has the maximum deformation.

Dye-stream experiments were also carried out for the channel for which the height in the absence of flow is $160\text{ }\mu\text{m}$ for the soft wall with two different shear moduli, shear modulus 18 kPa and $\Sigma = 4.48 \times 10^5$ and shear modulus 25 kPa and $\Sigma = 6.43 \times 10^5$. We were not able to carry out the experiments for catalyst concentration 2.25% because the Reynolds number for the destabilization of the dye-stream turned out to be larger than that achievable using our syringe pumps. For the gel with shear modulus 18 kPa and $\Sigma = 4.48 \times 10^5$, we observe oscillations in the dye stream at a Reynolds number of 333, and the dye stream breaks up at a Reynolds number of ~ 400 . For the gel with shear modulus 25 kPa and $\Sigma = 6.43 \times 10^5$, the dye stream shows oscillations at a Reynolds number of ~ 356 , but complete cross-stream mixing is not observed even at a Reynolds number of 444. In all cases, the instability

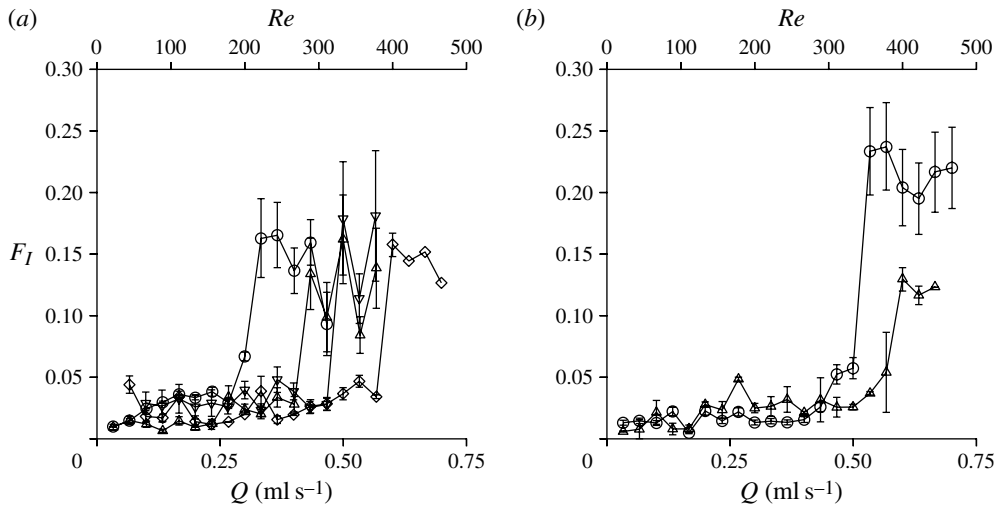


FIGURE 11. Root mean square of the laser intensity fluctuations as a function of the Reynolds number for a channel with height $100\ \mu\text{m}$ (a) and $160\ \mu\text{m}$ (b) in the absence of deformation, in which the soft wall is made of gel with shear modulus: \circ , 18 kPa and $\Sigma = 1.75 \times 10^5$; \triangle , 25 kPa and $\Sigma = 2.51 \times 10^5$; ∇ , 35 kPa and $\Sigma = 3.80 \times 10^5$; and \diamond , 54 kPa and $\Sigma = 5.86 \times 10^5$.

is first observed in the downstream contracting section of the channel, and not in the upstream expanding section where there is maximum deformation.

Wall oscillations were measured using laser scattering off microbeads embedded in the soft wall, as discussed in § 2. The scaled root mean square (r.m.s.) intensity fluctuation F_I , defined in (2.5), is shown as a function of the flow rate and the Reynolds number in figure 11. Even at low velocity, there is some non-zero value of F_I due to experimental noise. However, we see that there is a sharp and near-discontinuous change in F_I at a specific value of the Reynolds number. This value of the Reynolds number increases with the shear modulus of the soft wall, and it coincides with the Reynolds number at which the dye stream becomes unstable in the dye-stream experiments in figure 10.

4.2. Mixing

The mixing experiments were conducted in a channel with the Y inlet and outlet shown in figure 1(a). The images of the mixing experiments, captured using camera A in figure 2, at the locations shown in figure 1(a), are shown in figure 12 for the soft wall with four different gel shear moduli. Here, clear water is pumped through one of the inlets, and blue ink is pumped through the other inlet. At relatively low flow rates or Reynolds number, which are the top two sets of images in the figure, the flow is well segregated throughout the length of the channel. The two different streams enter symmetrically, remain distinct throughout the length of the channel and exit through the two different outlets. As the flow rate is increased, there is a threshold flow rate (or critical Reynolds number) at which there is a catastrophic breakdown of the streamlines and vigorous cross-stream mixing, as shown by the third set of images from the top in each figure. As in the case of the dye-stream experiments, cross-stream mixing is first observed at a location $L_2 \sim 1.5\ \text{cm}$ downstream of the entrance of the test section (third image from left in figure 12). Even when there is vigorous

cross-stream mixing downstream, there is little or no mixing at the location $L_1 \sim 5$ mm downstream from the entrance. As the Reynolds number is further increased, the cross-stream mixing is enhanced, until there is complete mixing across the entire channel, as shown by the fourth and fifth sets of images from the top in each of the sub-figures in figure 12. Even though the mixing is complete at the downstream locations L_2 and L_3 , there is only partial mixing at the location L_1 5 mm downstream of the entrance of the test section. There is no mixing at the location L_0 in the development section 2 mm upstream of the test section, indicating that the flow through a hard channel does not mix at this flow rate.

The threshold Reynolds number for the onset of cross-stream mixing is the same as that in the dye-stream experiments in a micro-channel of height 100 μm in the previous subsection, which is ~ 200 for the softest gel with shear modulus 18 kPa and $\Sigma = 1.75 \times 10^5$, ~ 289 for the gel with shear modulus 25 kPa and $\Sigma = 2.51 \times 10^5$, ~ 311 for the gel with shear modulus 35 kPa and $\Sigma = 3.80 \times 10^5$. For the soft wall with shear modulus 54 kPa and $\Sigma = 5.86 \times 10^5$, complete cross-stream mixing is observed at a Reynolds number of ~ 400 .

A quantitative measure of segregation based on image analysis, S_I is obtained from the four rectangles at different downstream locations shown in the top set of images in figure 12; the method of calculation is discussed in the § 2. The segregation index S_I varies between 0.5 (when there is no mixing between the two streams) and 0.0 (when there is complete mixing).

The segregation index at different locations from image analysis is shown in figure 13. Here, the error bars show the standard deviation of the variation of the segregation index with time. There is a clear transition in the segregation index at the downstream locations L_2 and L_3 which are 1.5 and 2 cm from the entrance of the test section from a value near 0.5 to a value close to 0. Even when there is mixing at locations L_2 and L_3 , figure 13 shows that there is only partial mixing at location L_1 5 mm from the entrance of the test section, and there is no mixing at the location L_0 which is in the development section.

The results obtained for the segregation index on the basis of image analysis are in agreement with those obtained using the mixing index (2.9) shown in figure 14. Here, the error bars show the standard deviation of the fluctuations of the mixing index with time. There is a sharp, near-discontinuous increase in the mixing index from a value close to zero, indicating no lateral mixing between the fluid in the two outlet streams in figure 1(a), to a value close to one, indicating complete lateral mixing and equal concentrations in the two outlet streams in figure 1(a). The Reynolds number for the transition is in agreement with that in figure 13 for the decrease in the segregation index at the downstream locations. At the Reynolds number of ~ 200 for the transition in figures 13 and 14 for the softest gels, the flow velocity is $\sim 1 \text{ m s}^{-1}$, and the residence time of the fluid in the channel is ~ 30 ms in the test section. Even within this short residence time, there is near complete mixing across the entire width of $W = 1.5$ mm. This is about five orders of magnitude lower than the mixing time due to diffusion, which is $(W^2/D) \sim 10^3$ s if we assume a relatively high value of $D = 10^{-9} \text{ m}^2 \text{ s}^{-1}$ for the diffusion of small molecules in water.

The intermittency in the mixing is analysed using the Fourier spectra of the concentration fluctuations, which are shown in figure 5(b). Here, we compare the spectra obtained at the DI water outlet at different Reynolds numbers. The reference used is the spectrum obtained when premixed tannic acid of concentration 1.25 g cc^{-1} is pumped in through both inlets of the Y micro-channel. The reference premixed tannic acid was pumped at a Reynolds number of 200, but we also verified that there

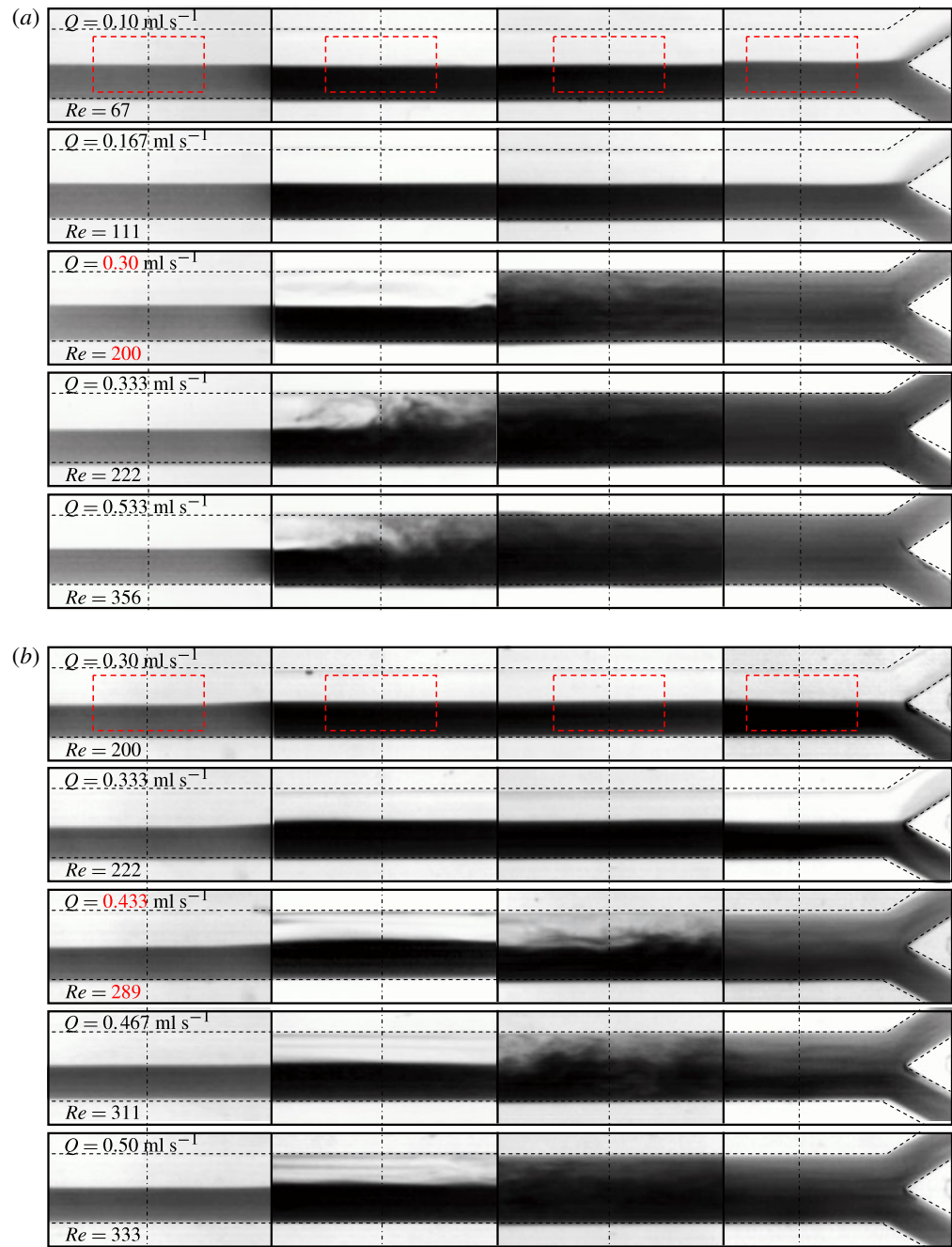


FIGURE 12. For caption see next page.

is little variation in the spectra for the premixed tannic acid as the Reynolds number is changed between 40 and 380.

For good mixing, one would expect the frequency spectrum to be the same as that for premixed tannic acid, while in the case of poor and intermittent mixing, there would be structure at low frequency in the power spectrum which is not present for

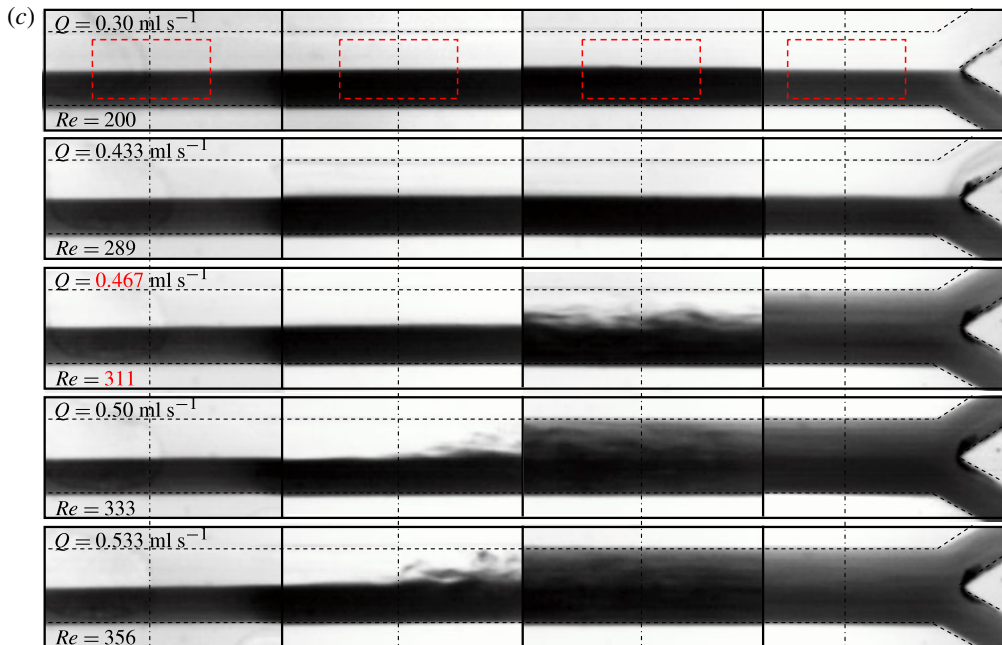


FIGURE 12. (Colour online) (contd). Images of flow in a Y micro-channel with dye-stream injected in one inlet and clear water in the other inlet at different Reynolds numbers. The soft wall of the micro-channel has shear modulus 18 kPa and $\Sigma = 1.75 \times 10^5$ (a), shear modulus 25 kPa and $\Sigma = 2.51 \times 10^5$ (b), and shear modulus 35 kPa and $\Sigma = 3.80 \times 10^5$ (c). The width of the micro-channel is 1.5 mm. From left to right, the images are centred at locations L_0 , L_1 , L_2 and L_3 in figure 1. The four rectangles in the top set of images are used for image analysis.

premixed tannic acid. The results are shown in figure 15 for the flow in a channel with soft wall made has shear modulus 18 kPa and $\Sigma = 1.75 \times 10^5$. These spectra show that there is intermittency at low frequency at a $Re = 200$ where the transition takes place, as well as at the $Re = 244$. However, the low-frequency structure disappears at $Re = 289$, and the spectrum is indistinguishable from premixed tannic solution when the Reynolds number is as low as 333. The same qualitative features are observed for the flow through a channel with soft wall made of shear modulus 25 kPa and $\Sigma = 2.51 \times 10^5$ shown in figure 16. In this case, there is intermittency at $Re = 244$ and 289, but the spectra are indistinguishable from premixed tannic acid at $Re = 333$ and 378.

It is important to note that the frequency spectra in figures 15 and 16 do not capture the frequency of the most unstable mode in the linear stability analysis, which is discussed in the following section. The linear analysis predicts that the frequency of the most unstable mode is of the order of 10^4 Hz, which is outside the range of our analysis since the data card records at a maximum frequency of 10^3 Hz. Only the low-frequency intermittency is measured here in the conductivity experiments.

The pressure difference across the test section is monitored by a side pressure port shown in figure 1(a). The pressure difference between the pressure transducer and the outlet is shown as a function of Reynolds number in figure 17. It should be noted that the pressure results from the channel with the Y inlet cannot be directly compared with numerical simulations because the surge tanks at the outlet are difficult

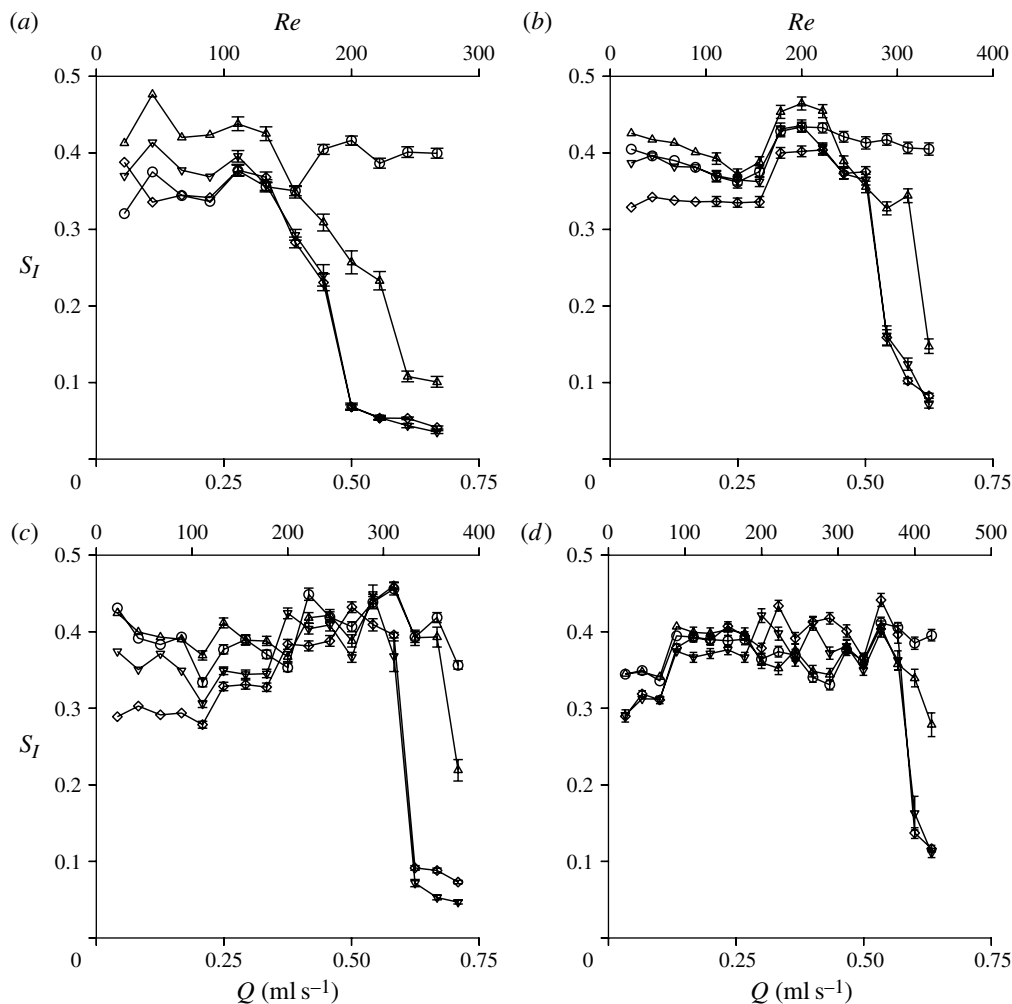


FIGURE 13. The segregation index obtained from image analysis S_I , equation (2.8) in § 2, as a function of flow rate and Reynolds number for four different channels in which the soft walls with shear modulus 18 kPa and $\Sigma = 1.75 \times 10^5$ (a), shear modulus 25 kPa and $\Sigma = 2.51 \times 10^5$ (b), shear modulus 35 kPa and $\Sigma = 3.80 \times 10^5$ (c) and shear modulus 54 kPa and $\Sigma = 5.86 \times 10^5$ (d) and at different downstream locations L_0 (○), L_1 (△), L_2 (▽) and L_3 (◇) in figure 1(a).

to simulate accurately. Therefore, while making theoretical comparisons in § 5, we will use different results obtained for the split flow inlet in figure 1(b) where the outlet is directly open to atmosphere. The results in figure 17 are used to demonstrate that there is no discontinuous change in the pressure drop at the transition from the laminar to well-mixed flow.

The results for a hard-walled channel, obtained using a catalyst concentration of 10 % ($G' = 0.5$ mPa), are shown by the \times in figure 17. In this case, the pressure difference increases approximately linearly with the flow rate, as expected for laminar flow. When the wall is made soft, the pressure difference is much smaller than that for a rigid walled channel, and it does not increase linearly with flow rate. This

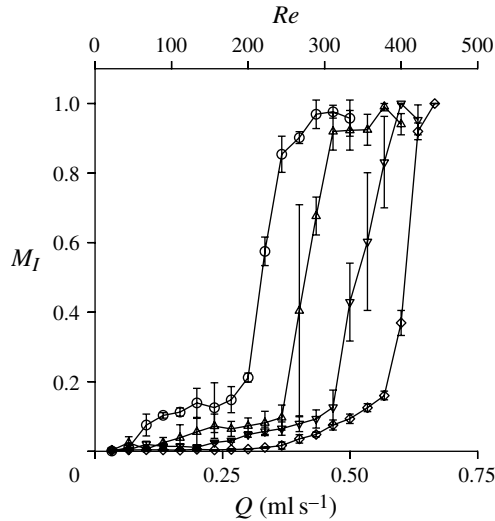


FIGURE 14. The mixing index obtained from concentration measurements M_I , equation (2.9) in § 2, as a function of flow rate and Reynolds number for four different gels in which the soft walls with shear modulus 18 kPa and $\Sigma = 1.75 \times 10^5$ (\circ), shear modulus 25 kPa and $\Sigma = 2.51 \times 10^5$ (\triangle), shear modulus 35 kPa and $\Sigma = 3.80 \times 10^5$ (∇) and shear modulus 54 kPa and $\Sigma = 5.86 \times 10^5$ (\diamond).

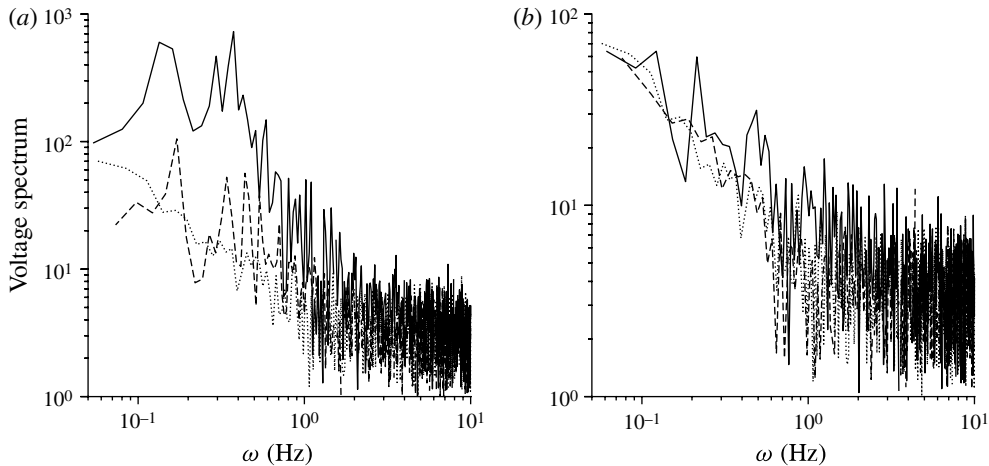


FIGURE 15. Frequency spectra of the measured outlet voltage for the flow through a channel with soft wall with shear modulus 18 kPa and $\Sigma = 2.51 \times 10^5$ for (a) $Re = 200$ (solid line), $Re = 244$ (dashed line) and (b) $Re = 289$ (solid line), $Re = 333$ (dashed line). In both panels, the dotted line shows the spectrum obtained when premixed tannic acid of equal concentration 1.25 g ml^{-1} is pumped into both inlets.

is due to an increasing deformation of the soft wall of the channel (Gordillo *et al.* 2004; Gervais *et al.* 2006; Hardy *et al.* 2009) with flow rate. The deformation is significant, as shown in the side view of the undeformed and deformed channels at different downstream locations for the softest gel, in figure 3. This results in a

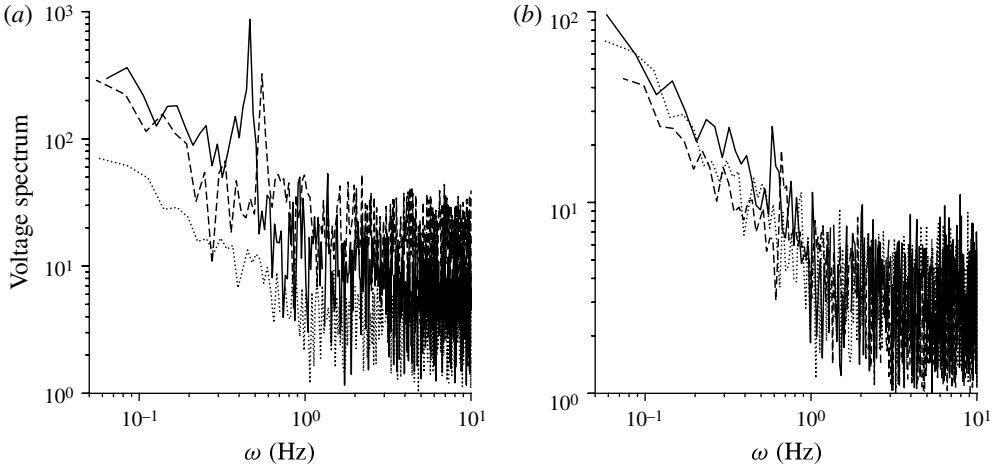


FIGURE 16. Frequency spectra of the measured outlet voltage for the flow through a channel with soft wall with shear modulus 25 kPa and $\Sigma = 2.51 \times 10^5$ for (a) $Re = 244$ (solid line), $Re = 289$ (dashed line), and (b) $Re = 333$ (solid line), $Re = 378$ (dashed line). In both figures, the dotted line shows the spectrum obtained when premixed tannic acid of equal concentration 1.25 g ml^{-1} is pumped into both inlets.

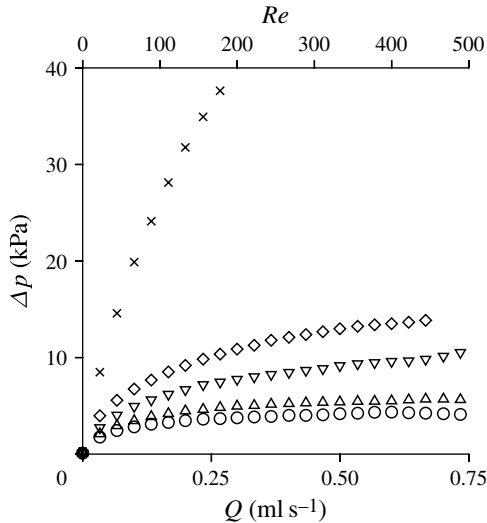


FIGURE 17. The pressure difference across the length of the channel as a function of flow rate and Reynolds number for channels of $100 \mu\text{m}$ height with the Y inlet (figure 1a) with soft walls that have \circ shear modulus 18 kPa and $\Sigma = 1.75 \times 10^5$, \triangle shear modulus 25 kPa and $\Sigma = 2.51 \times 10^5$, ∇ shear modulus 35 kPa and $\Sigma = 3.80 \times 10^5$, \diamond shear modulus 54 kPa and $\Sigma = 5.86 \times 10^5$, and \times a hard wall with shear modulus 0.5 mPa and $\Sigma = 5.4 \times 10^6$.

significant increase in the cross-sectional area, and a much lower pressure difference in comparison with a rigid channel of constant cross-section. An important observation is that the pressure difference increases only gradually as the Reynolds number is increased, and it does not show a discontinuous increase at the transition Reynolds

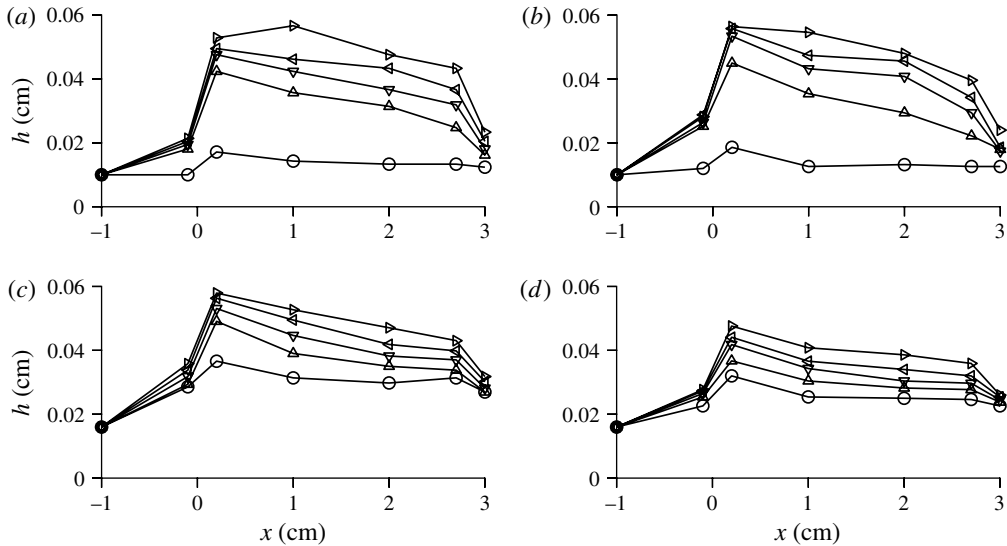


FIGURE 18. The height as a function of streamwise location x for Reynolds number 0 (\circ), 111 (\triangle), 200 (∇), 289 (\triangleleft) and 378 (\triangleright) for soft walls with shear modulus 18 kPa and $\Sigma = 1.75 \times 10^5$ (a,c), and shear modulus 25 kPa and $\Sigma = 2.51 \times 10^5$ (b,d) for channels with undeformed height 100 μm (a,b) and 160 μm (c,d). Note that the y-axis is magnified by a factor of 50 relative to the x-axis.

number. Therefore, near-complete cross-stream mixing is attained at very little cost in terms of additional pressure drop or energy requirement. This is in contrast to the laminar–turbulent transition in rigid tubes and channels, which are accompanied by a sharp and near-discontinuous increase in the pressure difference at transition.

5. Numerical results

5.1. Channel deformation

The detailed analysis of channel deformation, flow modification and the linear stability analysis is carried out for the channels with the two different heights, 100 and 160 μm , in the undeformed state. For the channels of height 100 μm in the absence of deformation, experiments were carried out with soft walls made with four different shear moduli, 18, 25, 35, 54 kPa, whereas for the channels of height 160 μm in the absence of deformation, we studied soft walls with two shear moduli, 18 and 25 kPa. The maximum channel height, $h_0 + h'$ in figure 7, obtained from the side views is shown at different streamwise locations for different Reynolds number and for the soft wall with two different shear moduli in figure 18. Here, the location $x = 0$ corresponds to the start of the test section, and positive x is downstream into the soft section. As expected, the deformation in the soft section decreases as the shear modulus of the soft wall is increased. It is also observed that the deformation in the hard section increases as the shear modulus of the soft wall is increased, due to the higher pressure in the hard section. There is a significant deformation from about 100 μm in the undeformed channel to ~ 600 μm at the highest Reynolds number of 378. However, even when the deformation is large, the slope of the wall is still small; the actual slope is 50 times smaller than the slope of the lines in figure 18, since the y-axis has been magnified by a factor of 50 in comparison with the scale on the x-axis. The maximum slope near

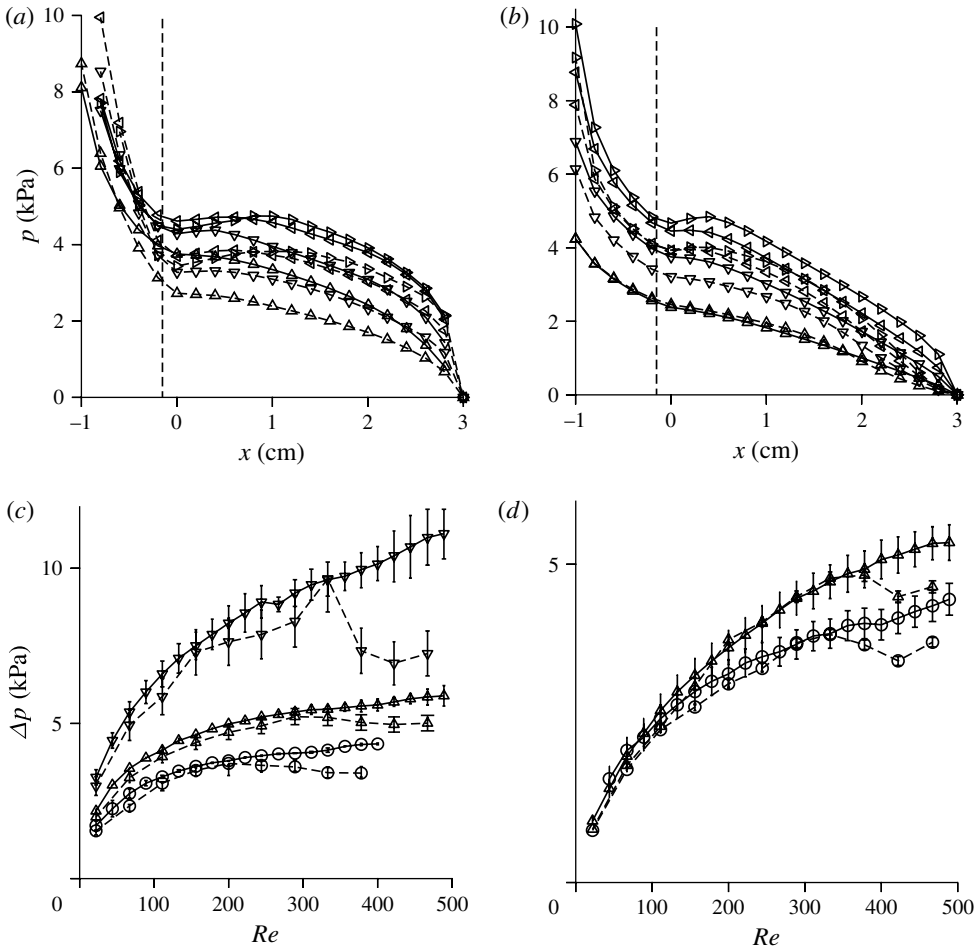


FIGURE 19. The difference in pressure between the streamwise location x and the outlet, as a function of the streamwise location, for Reynolds number 111 (Δ), 200 (∇), 289 (\triangleleft) and 378 (\triangleright) for soft walls with shear modulus 18 kPa, and $\Sigma = 1.75 \times 10^5$ (dashed line) and shear modulus 35 kPa and $\Sigma = 2.51 \times 10^5$ (solid line) for a channel with height $100 \mu\text{m}$ (a) and $160 \mu\text{m}$ (b) in the absence of deformation; and the pressure difference across the channel between the pressure transducer and the outlet as a function of Reynolds number for the soft wall with shear modulus 18 kPa and $\Sigma = 1.75 \times 10^5$ (\circ), shear modulus 25 kPa and $\Sigma = 2.51 \times 10^5$ (Δ) and shear modulus 35 kPa and $\Sigma = 3.80 \times 10^5$ (∇) from CFD simulations (dashed lines) and experiments (solid lines) for channels with height $100 \mu\text{m}$ (c) and $160 \mu\text{m}$ (d) in the absence of deformation. The vertical line in (a,b) shows the location of the pressure transducer.

the transition point for the soft wall with shear modulus 18 kPa and Reynolds number 200 is 0.09, while that near the transition point for a soft wall with shear modulus 25 kPa and Reynolds number 378 is 0.05.

The maximum height $h_0 + h'$ obtained in figure 18 is inserted into the cubic fit for the bottom wall shape shown in figure 7(b). This is then used in order to calculate the pressure variation along the length of the channel using the ANSYS FLUENT CFD simulation tool discussed in § 3. The results for the variation of the pressure as a function of the downstream distance along the channel are shown in figure 19(a,b).

Here, the pressure difference between the streamwise location x and the outlet is shown as a function of downstream distance x . The location $x = 0$ in this figure shows the start of the test section, and the vertical line shows the location of the pressure transducer. An interesting observation is the adverse pressure gradient in the test section ($x > 0$), due to the large expansion in the channel. Despite the large expansion, the velocity profiles from the CFD simulations, presented in figure 20, show no evidence of recirculation or reverse flow in the region of adverse pressure gradient.

The difference in pressure between the pressure transducer and the outlet obtained from the simulations (figure 19*a,b*), is compared with the experimental results in figure 19*(c,d)*. The error bars in the experimental results correspond to the standard deviation over three independent runs. The error bars in the theoretical pressure differences are due to the uncertainties in the measurement of the channel height from the images in figure 3. The minimum length that can be measured from these images is 5 μm , and so there is an uncertainty of $\sim 10 \mu\text{m}$ in the height measurement. At constant flow rate, the pressure drop is proportional to the inverse of the cube of the characteristic length, and so the uncertainty in the height results in an uncertainty of between 5–10 % in the pressure difference. This figure shows that the experimental and simulation pressures differences are in very good agreement at low Reynolds numbers. However, for Reynolds numbers higher than those for which a transition is observed in the dye-stream experiments, the pressure difference from the simulations is significantly lower than that from the experiments. The Reynolds number at which the theoretical and experimental pressure drops diverge is about the same as that where the dye-stream experiments in figure 10 show a breakup of the dye stream; these are compared in figure 29.

The CFD simulations also provide the detailed velocity profile throughout the channel. For the linear stability analysis, we focus on the x – z plane in figure 2, the plane of symmetry in the spanwise direction, whose projections are the vertical lines in the cross-section figures in figure 8*(b)*. These velocity profiles at different downstream distances from the entrance of the test section for the wall with shear modulus 18 kPa and $\Sigma = 1.75 \times 10^5$ and at a Reynolds number of 289 based on the flow rate are shown in figure 20. The actual velocity, obtained at discrete points from the CFD simulations, is shown by the symbols in figure 20*(a)*. Also shown in figure 20*(a)* are the results of simulations with different grid resolutions, of 15, 20 and 30 μm . It is clear that there is a difference of $\sim 10\%$ between the results for 30 and 20 μm ; this is because a grid spacing of 30 μm gives a relatively coarse grid where there are between 10–20 grid points across the channel. However, there is very little difference, $\sim 3\%$, between the results for grid resolutions of 20 and 15 μm , indicating grid size independence. The variation in the pressure profiles (figure 19) is even smaller, only $\sim 1\%$, when the grid resolution is decreased from 20 to 15 μm ; the grid dependence is not shown in figure 19 because the different curves are indistinguishable. Since there is grid size independence below 20 μm , a grid size of 20 μm is used for all our results.

In figure 20*(b)*, the scaled velocity, which is the velocity divided by its average value (equation (3.37)) is shown as a function of the scaled height ($y/(h_0 + h')$), where h_0 and h' are defined in figure 7 for the deformed channel. The quartic polynomial fits and the parabolic profile for the fully developed flow in a channel of constant cross-section are also shown. An important conclusion is that there is no velocity reversal or recirculation in all of the velocity profiles we have considered so far. So the dye-stream breakup is not due to velocity reversal or backflow. The velocity profile

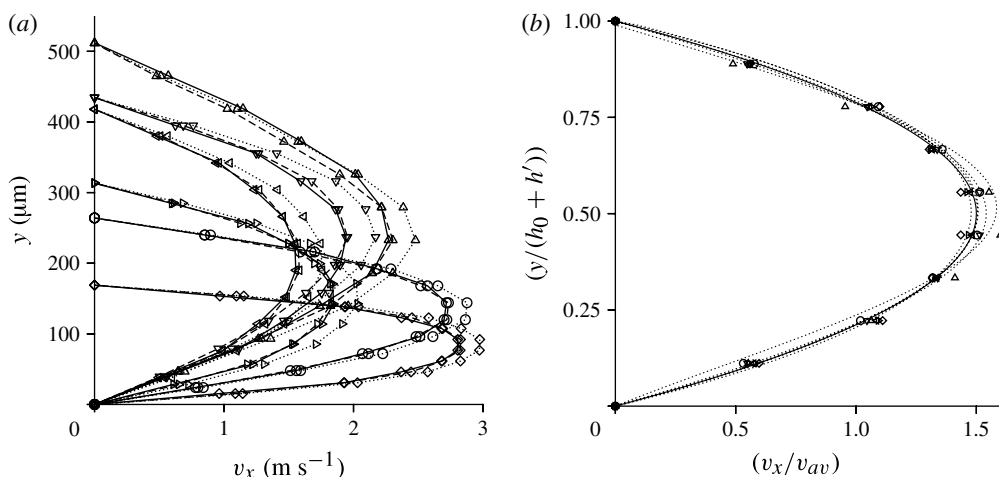


FIGURE 20. The mean velocity profiles for the flow through a channel in which the soft wall has shear modulus 25 kPa and $\Sigma = 2.51 \times 10^5$ for height $100 \mu\text{m}$ in the absence of deformation at a Reynolds number based on flow rate of 289, at distances $x = -0.1 \text{ cm}$ (\circ), 0.2 cm (\triangle), 1 cm (∇), 2 cm (\triangleleft), 2.7 cm (\triangleright) and at 3 cm (\diamond) from the start of the test section. The velocity (in m s^{-1}) as a function of the cross-stream distance in the simulation is shown by symbols in (a) for three different grid sizes, $15 \mu\text{m}$ (dashed line), $20 \mu\text{m}$ (solid line) and $30 \mu\text{m}$ (dotted line). The scaled velocity is shown as a function of the scaled cross-stream distance in (b) for the grid size of $20 \mu\text{m}$. The dotted lines in (b) show the quartic fits used for the linear stability analysis, and the solid line in (b) is the parabolic velocity profile.

is not very different from a parabolic profile even at the location 0.2 cm into the test section, where figure 8(a) shows that the deformation is a maximum. However, there are systematic differences. As expected, the velocity profile has a higher curvature at the centre than the parabolic profile in the diverging section of the channel, and is more plug-like with a lower curvature at the centre in the converging section. As we see in the next section, the small differences in the profile have a significant effect on the growth of perturbations.

The velocity profiles at different spanwise locations are shown at different downstream locations in figure 21. To place the figure in context, recall that the width of the channel in the spanwise direction is 1.5 mm , and the central plane (whose projection is the vertical line in the cross-sections in figure 8b) is 0.75 mm distant from either wall. The velocity profiles in figure 21 are shown at different z locations separated by $100 \mu\text{m}$ from the central plane in the spanwise direction. These figures show that at a relatively upstream locations 1 cm from the entrance, there is a significant slowing down as the distance from the central plane increases, and the maximum velocity at a distance of $z = \pm 300 \mu\text{m}$ is about one half of the value at the central plane $z = 0$. However, at the downstream locations $x = 2, 2.7$ and 3.0 cm from the inlet, there is relatively little variation of the velocity in the spanwise direction. In these cases, the channel width and the maximum velocity at $z = \pm 300 \mu\text{m}$ are not more than $\sim 10\%$ lower than that at $z = 0$, while the maximum velocity and channel width at $z = \pm 600 \mu\text{m}$ ($150 \mu\text{m}$ from the wall) are not more than 50% of that at $z = 0$. Thus, the spanwise velocity variations are small in the downstream converging section within a region of width $\pm 300 \mu\text{m}$ from the central plane.

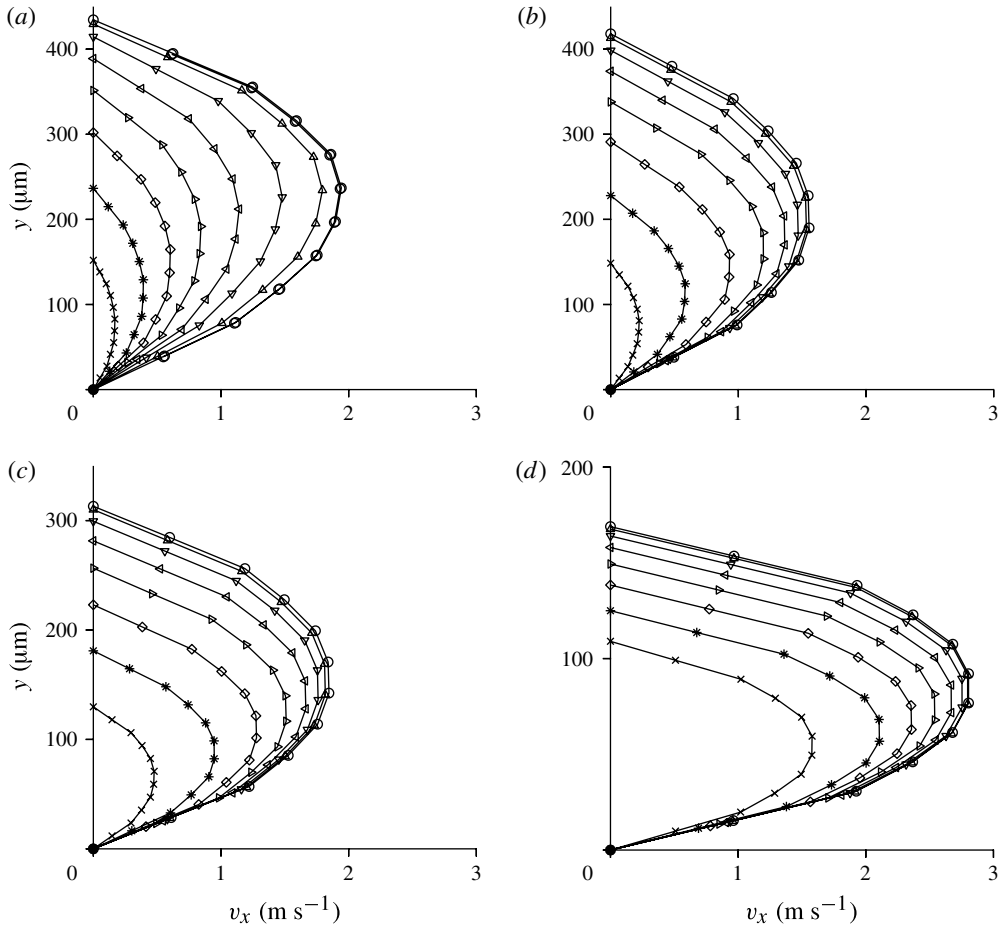


FIGURE 21. The mean velocity profiles for the flow through a channel in which the soft wall has shear modulus 25 kPa and $\Sigma = 2.51 \times 10^5$ for a channel with height 100 μm in the absence of deformation at a Reynolds number based on flow rate of 289, at different spanwise locations $z = 0$ (\circ), $z = \pm 100$ μm (Δ), $z = \pm 200$ μm (∇), $z = \pm 300$ μm (\triangleleft), $z = \pm 400$ μm (\triangleright), $z = \pm 500$ μm (\diamond), $z = \pm 600$ μm ($*$), $z = \pm 700$ μm (\times) and at different downstream locations $x = 1.0$ cm (a), $x = 2.0$ cm (b), $x = 2.7$ cm (c) and $x = 3.0$ cm (d) from the entrance to the test section.

Based on the mean velocity profiles, it is possible to define a local Reynolds number $Re' = (\rho v_{av}(h_0 + h')/\eta)$ for the velocity profiles shown in figure 20 where v_{av} is defined for each velocity profile using (3.37), and h_0 and h' are defined in figure 7. This is a local Reynolds number at the centreline shown in figure 3, and is different from the Reynolds number based on the flow rate in (2.1). The local Reynolds number is shown as a function of downstream position for different flow rates in figure 22. The local Reynolds number Re' is always larger than that based on the flow rate, because a larger velocity at the centreline shown in figure 8(b) is necessary to compensate for the slowing-down near the sidewalls in the z direction. The local Reynolds number at the location of maximum expansion could be as high as 2.5 times Re for a channel with height 100 μm in the absence of deformation, although it is not as large for a channel with height 160 μm in the absence of deformation, due to the smaller relative

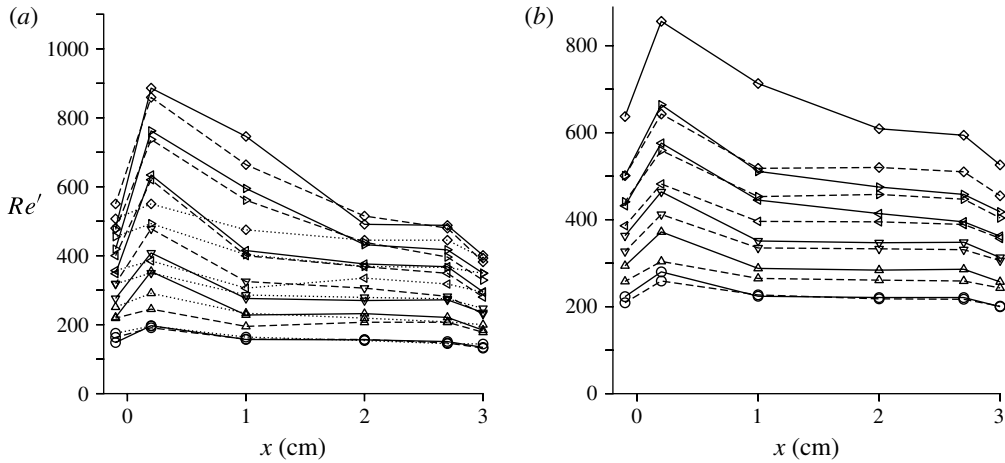


FIGURE 22. The local Reynolds number based on velocity profiles at the central plane of the channel in the spanwise direction as a function of downstream distance x for a channel with height $100\ \mu\text{m}$ (a) and $160\ \mu\text{m}$ (b) in the absence of deformation for $Re = 154$ (○), $Re = 200$ (△), $Re = 244$ (▽), $Re = 289$ (◁), $Re = 333$ (▷) and $Re = 378$ (◇) for a channel with height $100\ \mu\text{m}$ (a) and $160\ \mu\text{m}$ (b) in the absence of deformation for the soft wall with shear modulus 18 kPa and $\Sigma = 1.75 \times 10^5$ (solid line), shear modulus 25 kPa and $\Sigma = 2.51 \times 10^5$ (dashed line) and shear modulus 35 kPa and $\Sigma = 3.80 \times 10^5$ (dotted line).

deformation in the latter case. However, at the downstream locations for $x > 2$ cm, where the instability is first observed, the local Reynolds number is not more than 1.5 times Re .

5.2. Linear stability analysis

Before proceeding to solve the linear stability equations derived in § 3.2 to obtain the transition Reynolds number, it is important to examine the assumptions made in deriving this equation. The first assumption is that there is no velocity variation along the streamwise direction. This is valid only if the length scale for the velocity variation is larger than the wavelength of the unstable modes. Our analysis indicates that the most unstable modes have a wavenumber k of $O(1)$ when scaled by the inverse of the height of the undeformed channel h_0 . The flow development length scales as ratio of the channel height and the wall slope, (h_0/α) . The ratio of the wavelength of perturbations and the flow length scale is, therefore, $(k\alpha)$, where k is scaled by the channel height. The slope α be estimated from the maximum deformation in figure 18. The slope is quite large in the upstream diverging section for $0 \leq x \leq 0.2$ cm, where the height increases by $\sim 500\ \mu\text{m}$. However, both the experiments and the linear analysis applied at this location indicate that the flow is stable. Of more relevance is the downstream converging section, where the height decreases by $\sim 50\ \mu\text{m}$ over a distance of ~ 2.5 cm, and the slope is 0.02 or less. Consequently, the ratio of the wavelength of perturbation and the slope of the velocity profile is ~ 0.02 or less in the downstream converging section where perturbations are unstable, indicating that the neglect of the streamwise velocity variation is a good approximation in this region.

The justification for the nearly parallel flow approximation is as follows. If the channel wall has a small angle of inclination α , there is an error $O(\alpha)$ in the linear stability analysis when we assume a parallel flow, because the wall inclination has

been neglected. However, the modification of the mean velocity profile and pressure gradient are $O(\text{Re}^{-\alpha})$, where Re is the Reynolds number. In our case, the transition Reynolds number varies in the range 200–400, while the slope of the wall is ~ 0.02 or less in the downstream converging section. Therefore, it is a good approximation to retain terms of $O(\text{Re}^{-\alpha})$ which result in the mean velocity and pressure modification, and neglect terms of $O(\alpha)$ in the parallel flow approximation.

The strongest approximation made here is that of two-dimensional flow, which implies there are no variations in the spanwise direction. The width of the channels used is 1.5 mm, and two different heights, 100 and 160 μm , were used for the undeformed channel. So the ratio of width to height is between 9.5 and 15. When there is flow, the channel height increases because the soft wall deforms. At the downstream section where the instability is first observed (2.0 cm from the entrance of the test section) and for a Reynolds number of 289, the 100 μm channel height expands to $\sim 300 \mu\text{m}$, and the 160 μm channel height expands to $\sim 350 \mu\text{m}$. So the ratio of width and height is still ~ 5 for the smaller channel and 4 for the larger channel. We show later that the wavenumbers scale with the channel height, so the spanwise extent of the channel is significantly larger than the perturbation wavelength. Another concern is the assumption of a two-dimensional flow with no spanwise variations. As shown in figure 21, there is a significant variation of the velocity profile with spanwise position at the upstream locations < 1 cm from the entrance of the test section. However, at downstream locations > 2 cm from the entrance, there is less than 10 % the velocity profile within a region of thickness $\pm 300 \mu\text{m}$ from the central plane. Therefore, there is a central region of thickness 600 μm where the velocity is nearly a constant at the downstream locations where our stability analysis shows that the flow becomes unstable.

The linear stability analysis is used to determine the transition Reynolds number, where both k and ω in (3.20) and (3.21) are real at different downstream locations. These could be obtained by a temporal analysis, where we set a real k and then determine the Reynolds number where c is also real, or by a spatial analysis, where we set a real ω (kc) and determine the Reynolds number at which k is real. For the neutral modes, there is no difference in the predictions of the wavenumber and frequency between the local spatial and temporal analysis, provided the parallel flow approximation is valid. Gaster (1962) has shown that the frequency and growth rates for the temporal stability problem are related to the frequency and spatial amplification rates for the spatial stability problem near the neutral stability curve for a given wavenumber and Reynolds number. The frequencies in the two cases are nearly equal, the difference being quadratic in the growth rate. The ratio of the temporal and spatial growth rates is equal to the group velocity of the waves. In our present analysis, it is easier to identify the neutral stability curve by solving for real k .

It should be noted that in all of our results, we find that the least stable modes are propagating downstream, with a positive wave velocity and a positive group velocity. This is in agreement with the previous study of Gaurav & Shankar (2010) and with earlier studies, where the most unstable modes were found to propagate downstream for high Reynolds number. The analysis of Gaster (1962) also shows that near the neutral curve, the ratio of the temporal and spatial growth rates is equal to the group velocity of the waves. Therefore, just above the transition Reynolds number, growing modes for the temporal problem imply downstream travelling and amplifying spatial modes for the spatial problem.

The mean velocity profiles obtained as in figure 20, and the pressure profiles obtained as in figure 19, are used as inputs for the linear stability calculations.

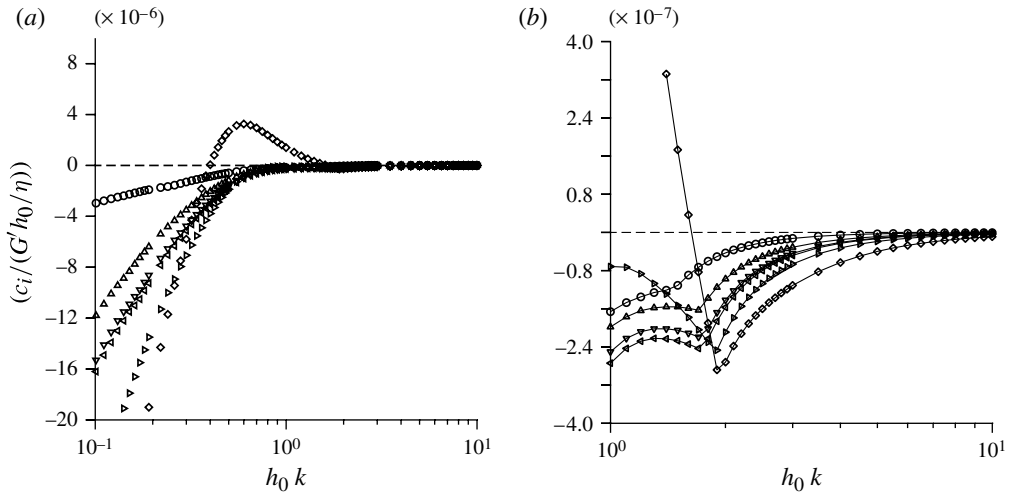


FIGURE 23. The imaginary part c_i of the wave speed c , scaled by $(G'h_0/\eta)$, for the least stable/most unstable solution as a function of the scaled wavenumber $h_0 k$ for a channel with height $100\ \mu\text{m}$ in the absence of deformation, with soft wall made with shear modulus $25\ \text{kPa}$ and $\Sigma = 2.51 \times 10^5$ for $Re = 244$, at different downstream locations $x = -0.1\ \text{cm}$ (\circ), $0.2\ \text{cm}$ (\triangle), $1.0\ \text{cm}$ (∇), $2.0\ \text{cm}$ (\triangleleft), $2.7\ \text{cm}$ (\triangleright) and $3.0\ \text{cm}$ (\diamond). In (b), the high wavenumber behaviour is magnified.

Equations (3.25), (3.29), (3.30) and (3.31), along with boundary conditions (3.32), (3.33), (3.34) and (3.36), are solved to obtain the c_r and c_i , the real and imaginary parts of the wave speed. The solutions for the wave speed is determined for a given wavenumber k , to obtain the spectrum. The solution for c with the largest imaginary part (least stable or most unstable mode) is then plotted as a function of the wavenumber k for each downstream location. The results for a channel with soft wall made with shear modulus $25\ \text{kPa}$ and $\Sigma = 2.51 \times 10^5$ at a Reynolds number of 244 for a channel with height $100\ \mu\text{m}$ in the absence of deformation, is shown in figure 23. This figure shows that the velocity profile at only one location, the channel exit at $x = 3.0\ \text{cm}$, has an unstable solution, while the velocity profiles at all other locations are stable. There are some features of the high wavenumber behaviour of c_i which are common to all of the results obtained here, which are shown in the magnified figure 23(b). In all cases, c_i first increases, passes through a maximum, decreases a little and then increases again to asymptote to the k -axis in the high k limit. The value of c_i at the intermediate maximum is negative for $x \leq 2.7\ \text{cm}$, but it becomes positive $x = 3.0\ \text{cm}$. In all cases, we observe that it is the intermediate local maximum at finite k , which is initially negative, that crosses the k -axis and becomes positive as the flow rate is increased. Therefore, in the following results, the magnitude and wavenumber of the local maximum are analysed as a function of downstream position and flow velocity.

The local maximum value of c_i in figure 23 is plotted as a function of downstream location for different Reynolds numbers in figure 24. These figures show that c_i is largest at the downstream end of the channel, and lowest at the location $x = 0.2\ \text{cm}$ where the deformation and local Reynolds number are largest. As the Reynolds number is increased, the velocity profile becomes unstable at progressively upstream locations. This is in agreement with experimental observations that the instability is

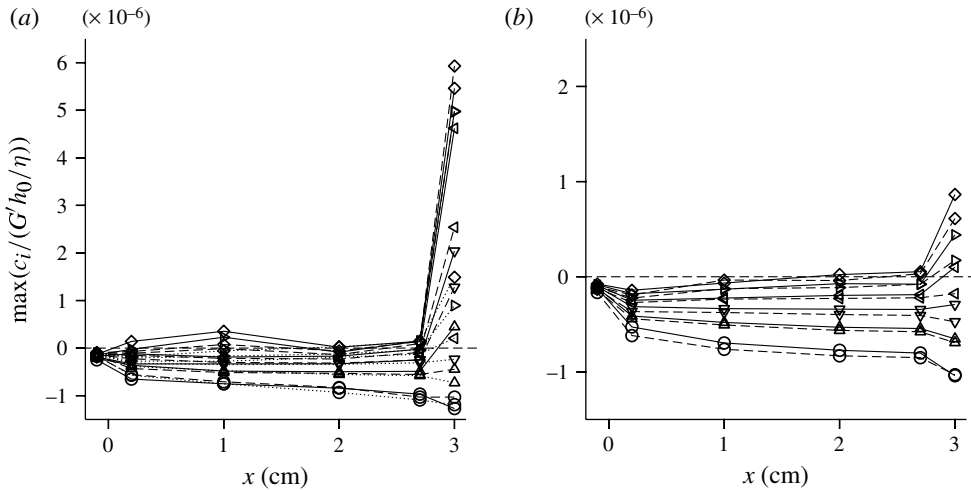


FIGURE 24. The maximum value of c_i , scaled by $(G'h_0/\eta)$ as a function of downstream distance x for a channel with height $100\ \mu\text{m}$ (a) and $160\ \mu\text{m}$ (b) in the absence of deformation for a flow with $Re = 111$ (\circ), $Re = 156$ (\triangle), $Re = 200$ (∇), $Re = 244$ (\triangleleft), $Re = 289$ (\triangleright) and $Re = 333$ (\diamond), in which the soft wall is made with shear modulus $18\ \text{kPa}$ and $\Sigma = 1.75 \times 10^5$ (—), shear modulus $25\ \text{kPa}$ and $\Sigma = 2.51 \times 10^5$ (— — —) and shear modulus $35\ \text{kPa}$ and $\Sigma = 3.80 \times 10^5$ (···).

first observed more than $2.0\ \text{cm}$ downstream of the entrance to the test section, where the channel is converging. The dye stream is observed to be laminar in the diverging section at the entrance of the channel.

The eigen-functions for the velocity perturbations in the fluid and the displacement field in the gel wall, shown in figure 25 provide insight into the destabilizing mechanism. The salient characteristic of the wall-mode eigenfunctions, which is the confinement of the velocity perturbations in the region close to the interface, is clearly observed in figure 25(a). This clearly confirms that the destabilizing mechanism in the present case is the wall mode instability due to the shear work done at the fluid–solid interface, and not due to Reynolds stresses in the bulk of the fluid, as expected for the inviscid instability. Theoretically, in the wall mode instability, perturbations are confined to a layer of thickness $Re^{-1/3}$ at the wall. This magnitude is in agreement with the results in figure 25, where we see that the wall layer thickness is ~ 0.15 times the channel height at a Reynolds number of 289 . However, the Reynolds number is too small to be able to recover the asymptotic scaling law (Shankar & Kumaran 2001a, 2002). There is also confinement of the displacement perturbations in the solid to a thin layer near the surface, as shown in figure 25(b). This is due to a different reason, which is the relatively large thickness of the solid layer in comparison to the fluid layer. The soft gel wall in our experiments is $2\ \text{mm}$ in thickness, which is significantly larger than the undeformed fluid layer ($100\ \mu\text{m}$), as well as the wavelength of the unstable modes. So the solid layer is effectively like an infinite medium, in which the depth of penetration of the perturbations is set by the wavelength. Owing to this, the displacement perturbations are confined to a relatively thin zone near the surface.

The results of the linear stability analysis can be quantitatively related to experimental results. For a channel with height $100\ \mu\text{m}$ in the absence of deformation,

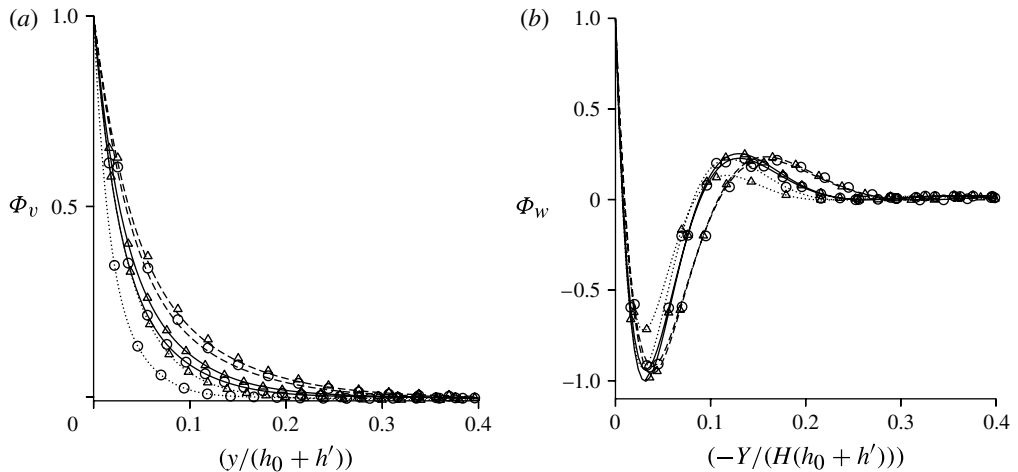


FIGURE 25. The real parts of the eigenfunctions for the fluid velocity perturbation $\Phi_v = (\tilde{v}_x/\tilde{v}_x|_{y=0})$ (a), and the wall displacement field $\Phi_w = (\tilde{w}_x/\tilde{w}_x|_{y=0})$ (b), as a function of the distance from the fluid–solid interface scaled by the fluid thickness $(h_0 + h')$ (a) and solid thickness $H(h_0 + h')$ (b) for a channel with height $100\ \mu\text{m}$ in the absence of deformation and for the soft wall with shear modulus $18\ \text{kPa}$ and $\Sigma = 1.75 \times 10^5$ and $Re = 244$ (dashed line), shear modulus $25\ \text{kPa}$ and $\Sigma = 2.51 \times 10^5$ and $Re = 289$ (solid line) and shear modulus $35\ \text{kPa}$ and $\Sigma = 3.80 \times 10^5$ and $Re = 333$ (dotted line) for the most unstable mode c_i at the location $x = 2\ \text{cm}$ (○) and $3.0\ \text{cm}$ (Δ) from the inlet of the channel. In both parts, \tilde{v}_x and \tilde{w}_x are divided by their value at the wall $y = 0$. Scaled this way, the imaginary parts of the eigenfunctions are smaller by a factor 10^{-2} in comparison with the real parts, and so they are not explicitly shown. The displacement and velocity fields are shown only up to a scaled distance of 0.4 , from the interface since they decay to zero beyond this point.

for the soft wall made with shear modulus $18\ \text{kPa}$ and $\Sigma = 1.75 \times 10^5$, the value of c_i first becomes positive at the outlet $x = 3.0\ \text{cm}$ for $Re = 156$, while the c_i becomes positive within the channel at $x = 2.0\ \text{cm}$ for $Re = 244$. In experiments, the instability of the dye stream is first observed at a Reynolds number of 178 , and there is breakup of the dye stream at $Re = 200$. For the soft wall with shear modulus $25\ \text{kPa}$ and $\Sigma = 2.51 \times 10^5$, c_i at the exit $x = 3.0\ \text{cm}$ becomes positive for $Re = 200$, while that at $x = 2.0\ \text{cm}$ becomes positive for $Re = 289$. In experiments, we observe that the dye stream breaks up for $Re = 244$. For the soft wall with shear modulus $35\ \text{kPa}$ and $\Sigma = 3.80 \times 10^5$, the flow becomes unstable at the exit at $Re = 244$, and the flow at $x = 2$ becomes unstable at $Re = 333$. In the experiments, the dye stream becomes unstable at $Re = 289$ and there is complete breakup of the dye stream at $Re = 333$. Thus, there is a clear correlation between the growth of perturbations predicted by the linear stability analysis and the breakup of the dye stream in experiments.

It is important to note that the unstable modes shown in figure 23 are obtained only when the modification to the mean velocity profile in figure 20 and the pressure gradient from the CFD simulation shown in figure 19 are incorporated in the linear stability analysis. Whereas there is not much modification of the mean velocity profile as shown in figure 20, there is a substantial modification of the pressure profiles. The actual pressure gradient (dp/dx) , scaled by (G'/h_0) at different downstream locations from the CFD simulations are compared with the theoretical prediction obtained from the local average velocity and height assuming using the plane Poiseuille law in

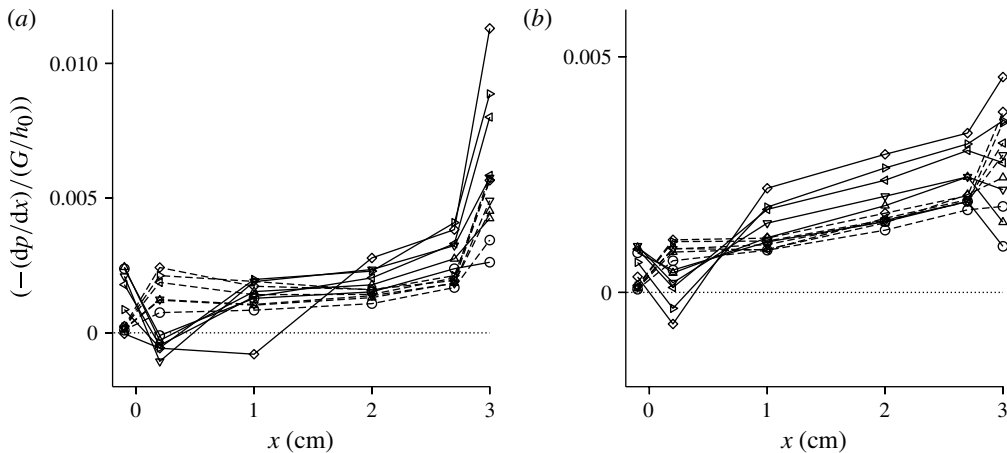


FIGURE 26. The scaled pressure gradient, $(-dp/dx)/(G'/h_0)$, as a function of streamwise location x for Reynolds number 111 (\circ), 200 (\triangle), 244 (∇), 289 (\triangleleft), 333 (\triangleright) and 378 (\diamond), for soft walls with shear modulus 18 kPa and $\Sigma = 1.75 \times 10^5$ (a) and shear modulus 35 kPa and $\Sigma = 3.80 \times 10^5$ (b) for a channel with height 100 μm in the absence of deformation. The solid lines show the actual pressure gradient from the CFD simulations in the deformed channel and the dashed lines show the theoretical prediction from the plane Poiseuille law for a parallel flow with the same average flow rate and channel height as the actual velocity profile in figure 20.

figure 26. Clearly, the modification in the pressure gradient is significantly higher than that in the velocity profile. In the expanding section, the pressure gradient becomes negative due to the decelerating flow. In contrast, in the downstream converging section, the pressure gradient is higher than that for a parabolic flow with the same profile as that in figure 20. In agreement with earlier predictions (Shankar & Kumaran 1999), the linear stability results show that flow in the diverging section is more stable than the parabolic flow, whereas that in the converging section is more unstable than the parabolic flow.

To investigate the effect of modification in the flow profile and pressure gradient on the instability, we have carried out a set of linear stability calculations using:

- (a) the parabolic approximation for the mean velocity instead of the quartic approximation; and
- (b) the parabolic approximation for the velocity profile with the pressure and velocity related by the plane Poiseuille law.

The results of the linear stability analysis for the highest Reynolds number of 378 used here are shown in figure 27 for soft walls with three different shear moduli. When the parabolic fit is used for the velocity profile and the pressure gradient from the CFD simulations is used, we find that the system does become unstable, but the growth rate is smaller than that when the quartic fit is used. In contrast, when the parabolic fit is used for the velocity profile and the Poiseuille law is used for the pressure–velocity relationship, we find that the flow is always stable. Thus, we find that it is essential to include the modification of the pressure gradient due to deformation in order to predict an instability; perturbations are always stable for the parabolic flow with linear pressure gradient obtained from the plane Poiseuille law when the local Reynolds number is used. Use of a quartic approximation does amplify the growth rates, but the

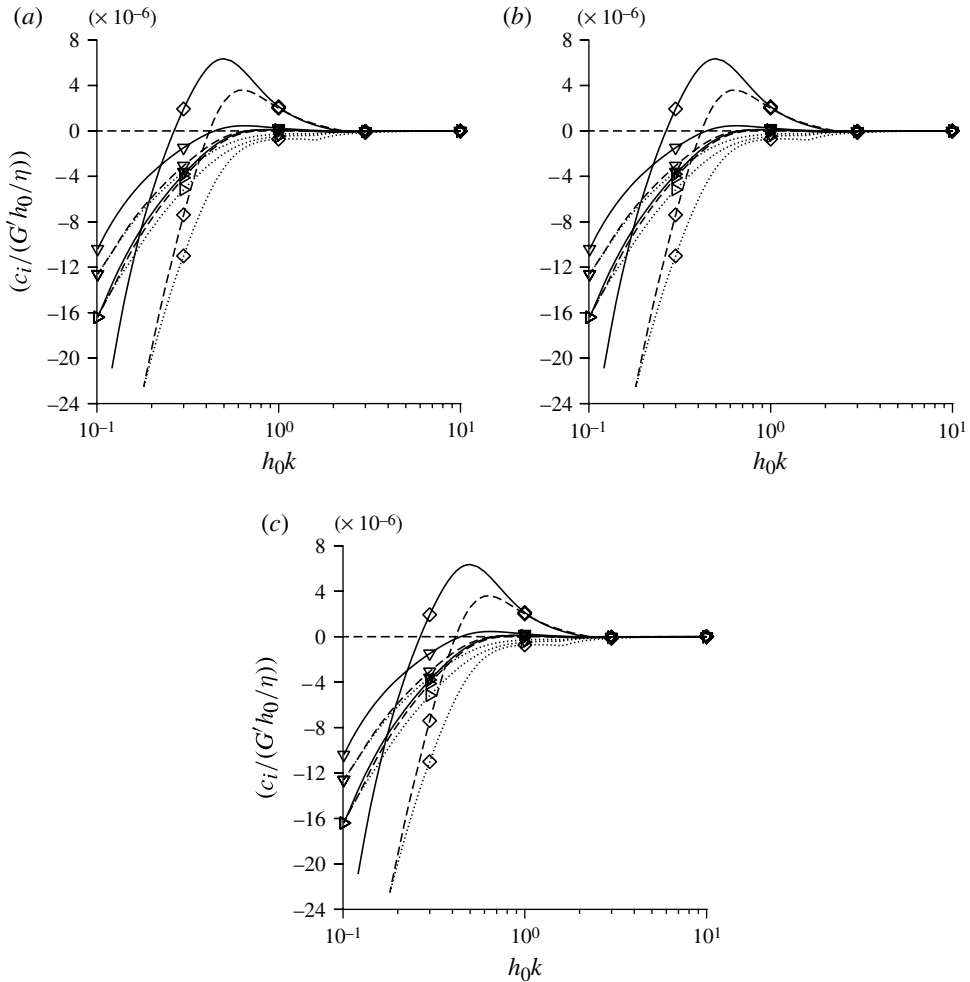


FIGURE 27. The imaginary part c_i of the wave speed c for the least stable/most unstable solution, scaled by $(G'h_0/\eta)$, as a function of the scaled wavenumber h_0k for a channel with height $100\ \mu\text{m}$ in the absence of deformation in which the soft wall is made with shear modulus $18\ \text{kPa}$ and $\Sigma = 1.75 \times 10^5$ (a), shear modulus $25\ \text{kPa}$ and $\Sigma = 2.51 \times 10^5$ (b) and shear modulus $35\ \text{kPa}$ and $\Sigma = 3.80 \times 10^5$ (c) for $Re = 378$ at different downstream locations $1.0\ \text{cm}$ (∇), $2.0\ \text{cm}$ (\triangleleft) and $3.0\ \text{cm}$ (\diamond). The solid and dashed lines show the results for the pressure gradient from the CFD code and the quartic and parabolic approximations for the velocity profiles, respectively, and the dotted line shows the results when the parabolic approximation is used for the velocity profile and the plane Poiseuille law is used to calculate the pressure gradient.

flow does become unstable even when a parabolic fit is used for the velocity profile when the actual pressure gradient from CFD simulations is used.

The wavenumber of the most unstable perturbation is shown in figure 28(a). Note that the undeformed channel height is used for scaling the wavenumber in our linear stability analysis. The wavenumber k decreases as c_i increases, but it varies in a relatively small range between 0.5 and 2.0 . Thus, the most unstable modes have wavelength comparable with the channel height. Figure 28(b) shows

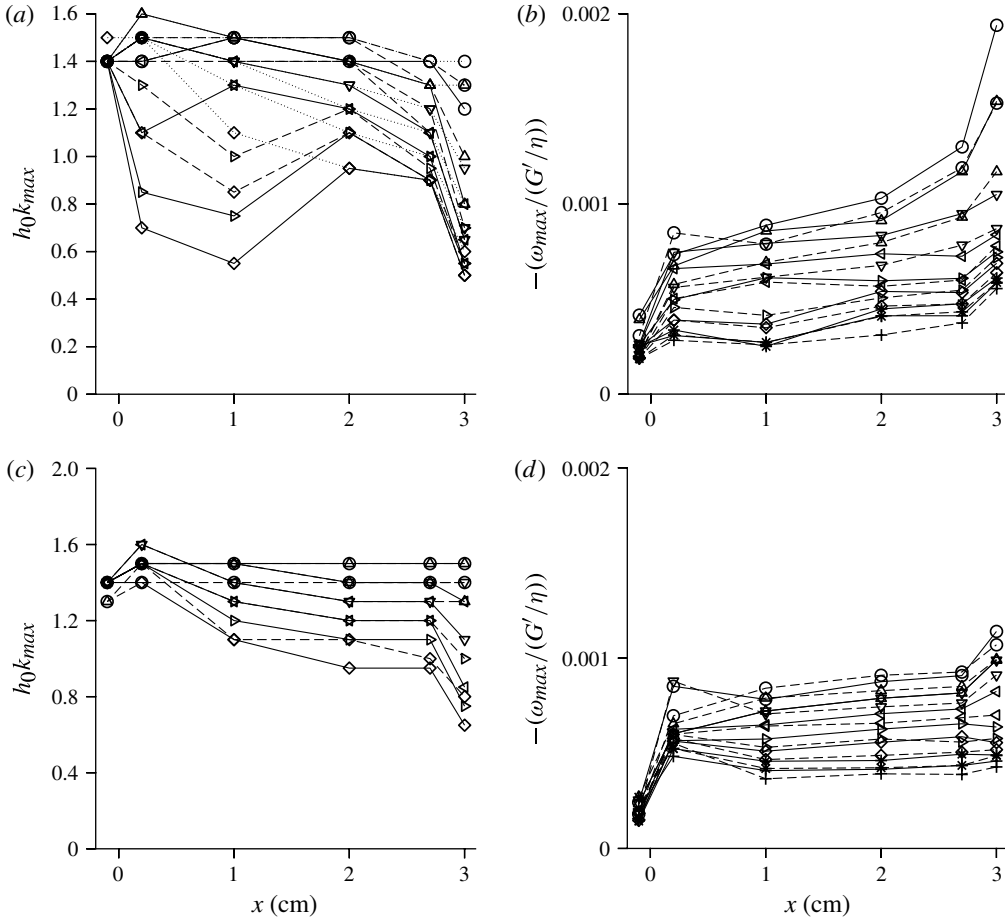


FIGURE 28. The scaled wavenumber $h_0 k_{max}$ at which c_i is a maximum (a,c), and the negative of the scaled frequency $-(\omega_{max}/(G'/\eta))$ of the least stable/most unstable mode (b,d) as a function of downstream location for $Re = 111$ (\circ), $Re = 156$ (\triangle), $Re = 200$ (∇), $Re = 244$ (\triangleleft), $Re = 289$ (\triangleright) and $Re = 333$ (\diamond) for a soft wall with shear modulus 18 kPa and $\Sigma = 1.75 \times 10^5$ (solid line), shear modulus 25 kPa and $\Sigma = 2.51 \times 10^5$ (dashed line) and shear modulus 35 kPa and $\Sigma = 3.80 \times 10^5$ (dotted line) for a channel with height 100 μm (a,b) and 160 μm (c,d) in the absence of deformation.

the frequency of the least stable/most unstable perturbation scaled by (G'/η) . The scaled frequency is $\sim 2 \times 10^{-3}$, which implies that the dimensional frequency is $2 \times 10^{-3} \times (G'/\eta) \sim 3.6 \times 10^4 \text{ s}^{-1}$ for the softest wall with shear modulus 18 kPa and $\eta = 10^{-3} \text{ kg m}^{-1} \text{ s}^{-1}$. Clearly, these are very high-frequency perturbations which will be a challenge to observe experimentally, even with high-speed imaging.

An important issue is whether it is possible that the dye-stream oscillations downstream could be due to perturbations becoming unstable upstream, and being convected before the growth is apparent. Experimentally, this is not the case because we see a rather abrupt breakup of the dye stream, and there is no evidence of sinusoidal waves in the dye stream slowly increasing in amplitude until it reaches the downstream converging section. The resolution of our camera is 1280×960 pixels, and the area imaged is $\sim 3 \text{ mm}$. Consequently, along the smallest dimension, our resolution

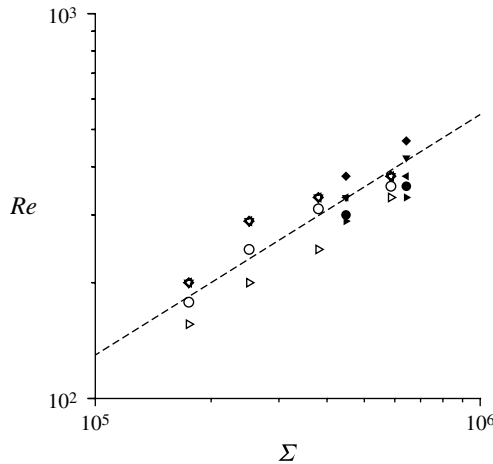


FIGURE 29. The Reynolds number for: \circ , breakup of the dye stream (figure 10); ∇ , detection of wall oscillations in laser scattering (figure 11); \triangleleft , underestimation of experimental pressure by CFD prediction (figure 19*c,d*); \triangleright , positive c_i at the downstream end $x = 3.0$ cm (figure 24); and \diamond , positive c_i at location $x = 2$ cm (figure 24) as a function of the parameter $\Sigma = (\rho G' h_0^2 / \eta^2)$. The open and filled symbols are the results from the channel with height 100 μm and 160 μm in the absence of deformation, respectively.

is $\sim 3 \mu\text{m}$. We will be unable to resolve disturbances only if they are less than 3 μm over a channel width of 1.5 mm. In practice, we find we are able to resolve distances to within $\pm 5 \mu\text{m}$ accurately. This gives a lower bound amplitude of $\sim 1\%$ for our detection capability; if the disturbance is less than this, we will not be able to detect it. So our detection threshold is sufficiently small that there will not be large regions where disturbances can grow undetected.

The spatial growth rate of disturbances can be examined theoretically from the group velocity. The temporal and spatial growth rates are related through the group velocity of the waves (Gaster 1962) through the relation

$$\frac{k_r c_i|_T}{k_i|_S} = -\frac{\partial \omega}{\partial k_r} \quad (5.1)$$

where T denotes the temporal stability problem and S the spatial stability problem, and ω is the frequency of the most unstable modes at transition. The group velocity on the right-hand side of (5.1) can be estimated as $10^{-3}(G'h_0/\eta)$, because the frequency in figure 28 is $10^{-3}(G'h_0/\eta)$ in scaled units and the wavenumber is $O(1)$. For $G' \sim 10$ kPa, $h_0 \sim 100 \mu\text{m}$ and $\eta \sim 10^{-3} \text{ kg m}^{-1} \text{ s}^{-1}$, the wave speed is $\sim 1 \text{ m s}^{-1}$, which is comparable with the mean flow velocity. The imaginary part of the wave speed can be estimated as $c_i \sim 10^{-6}(G'h_0/\eta)$ from figure 24 and $k_r \sim h_0^{-1}$ from figure 28. From this, we find that the spatial growth rate $k_i \sim 10^2 \text{ m}^{-1}$. Thus, the length scale for the spatial growth of perturbations is 1 cm, and disturbances cannot grow undetected over a distance of 2 cm from the upstream diverging section to the downstream converging section.

The experimental results of the previous section are compared with the results of the linear stability analysis in figure 29, where the transition Reynolds number is shown as a function of the parameter $\Sigma = (\rho G' h_0^2 / \eta^2)$, where h_0 is the height of the undeformed channel. There is close agreement between the results for the breakup of the dye

stream and onset of wall oscillations in experiments, as well as the Reynolds number at which there is a divergence between the pressure difference across the channel in the experiments and CFD simulations. The experimental results are bounded, above and below, by the theoretical Reynolds number for instability at the outlet $x = 3.0$ cm and the location $x = 2.0$ cm, respectively. The experimental dye stream and wall oscillation data for the channel with undeformed height $160\text{ }\mu\text{m}$ are also shown in figure 29. The dashed line, which shows the power law $Re = 0.09725\Sigma^{5/8}$, provides a good fit for the present data as well, although it must be cautioned that we do not have data for even a decade variation in Σ . The $\Sigma^{5/8}$ scaling law was obtained in Verma & Kumaran (2012) by recognizing that when there is a small inclination α at the wall, the flow modification is proportional to $Re\alpha$. The velocity gradient near the wall was related to the Reynolds number and the angle of inclination in the limit $Re\alpha \gg 1$, and α was related to the pressure gradient and the shear modulus. These qualitative arguments apply in the present configuration as well and, therefore, a scaling law of the form $Re \propto \Sigma^{5/8}$ is expected. Our numerical analysis shows that the Re versus Σ relationship can be predicted quantitatively on the basis of flow simulations and linear stability analysis.

6. Conclusions

The important conclusions of the present study are as follows.

- (a) The experiments on the breakup of a dye stream in a micro-channel with one soft wall have demonstrated that it is practically feasible to trigger a dynamical instability in microfluidic devices at a Reynolds number much lower than the transition Reynolds number of ~ 1200 in rigid channels.
- (b) The instability is tunable, and the transition Reynolds number decreases as the shear modulus of the soft wall is decreased. The transition Reynolds number is ~ 200 for the walls with the lowest shear modulus in the experiments.
- (c) In experiments, it has been demonstrated that the Reynolds number for the breakup of the instability coincides with the onset of wall oscillations detected by laser scattering off fluorescent beads in the wall.
- (d) From conductance spectra measurements, we find that the quality of mixing between the two streams is close to that for premixed solutions at Reynolds number as low as 300 for the soft walls with the lowest shear modulus used here.
- (e) The deformed shape of the channel was recorded from the experiments and reconstructed, and flow simulations were carried using Fluent CFD package. The pressure drop predicted by the simulations was close to the experimental pressure drop when the flow is laminar, but the experimental pressure drop was significantly higher than the simulation prediction after dye-stream breakup.
- (f) The velocity profiles and pressure gradient from the simulations were used in a linear stability analysis for the flow past a flexible wall using the parallel flow approximation. The predictions for the Reynolds number and streamwise location of the instability are in quantitative agreement with experimental observations.
- (g) From the linear stability calculations we find that the flow first becomes unstable in the downstream converging section of the channel where the slope of the wall is relatively small, and not in the upstream diverging section where the deformation and the local Reynolds number are largest.
- (h) The modification of the parabolic profile and the pressure gradient due to the convergence of the channel is necessary for destabilizing the flow. Linear stability

calculations indicate that the flow is stable for Reynolds numbers up to 1000 for a parabolic flow with the pressure gradient given by the plane Poiseuille law.

Thus, detailed comparison of experimental results and theoretical calculations with no fitted parameters has demonstrated unambiguously that the dye-stream breakup is due to a dynamical instability due to dynamical interaction between the fluid and the soft wall. The transition Reynolds number is fortuitously decreased due to the natural deformation of the soft wall, and the resulting change in the velocity profile and pressure gradient.

The present work is the first demonstration of ‘soft mixing’ in a micro-channel: the practical realization of a dynamical instability to reduce the transition Reynolds numbers. This could have significant implications for the flow past soft surfaces in, for example, the cardiovascular system where the conduits are made of soft materials. This could also be important in enhancing mixing in microfluidic devices, where slow mixing due to molecular diffusion in a laminar flow has been an obstacle in developing efficient lab-on-a-chip technologies. This instability mechanism provides a new strategy for enhancing mixing which has the advantages of passive strategies (no moving parts) and active strategies (spontaneous wall motion due to a dynamical instability of the base flow) at very little additional pressure drop or energy requirement. Owing to the catastrophic breakup of the base laminar flow, the mixing efficiency is much higher than that for passive strategies. For the flow velocities or up to 1 m s^{-1} used here, we find complete mixing for a residence time of only $\sim 30 \text{ ms}$ in a channel of length 3 cm, which is five orders of magnitude lower than that for molecular diffusion across a width of 1.5 mm.

We have also developed a framework which involves the prediction of the laminar flow and pressure gradient in a deformed channel, and the use of linear stability analysis to predict the threshold Reynolds number and downstream location of the instability. When coupled with a solid-mechanics framework for predicting wall deformation, it is possible to develop a systematic first-principles strategy for analysing flow in biological systems with soft walls. This can also be used for the design of low-cost microfluidic devices which use soft walls to transcend the technological barrier of mixing due to molecular diffusion in laminar flows in microfluidic devices.

Acknowledgements

The authors would like to thank the Department of Science and Technology, Government of India, for financial support. The authors would also like to thank Professor V. Shankar and Dr Gaurav for help with the linear analysis, and for instructive discussions.

Appendix A. Fabrication

The three ‘hard walls’ of the channel are cast using the standard PDMS soft lithography procedure. A negative of the channel is fabricated on a silicon wafer using SU8 photoresist, the prepolymer is poured onto this negative and cross-linked by standard procedures (Verma & Kumaran 2012). After cross-linking, the polymer is peeled off to provide an open channel, as shown in figure 30(a). The fourth wall of the channel was prepared separately as a film of thickness 2 mm, as shown in figure 30(b). This wall consists of two parts, one made of hard gel for the flow development section and the second made of soft gel for the test section. These two sections cannot be made separately and joined, since this results in a variation in the thickness at the joint.

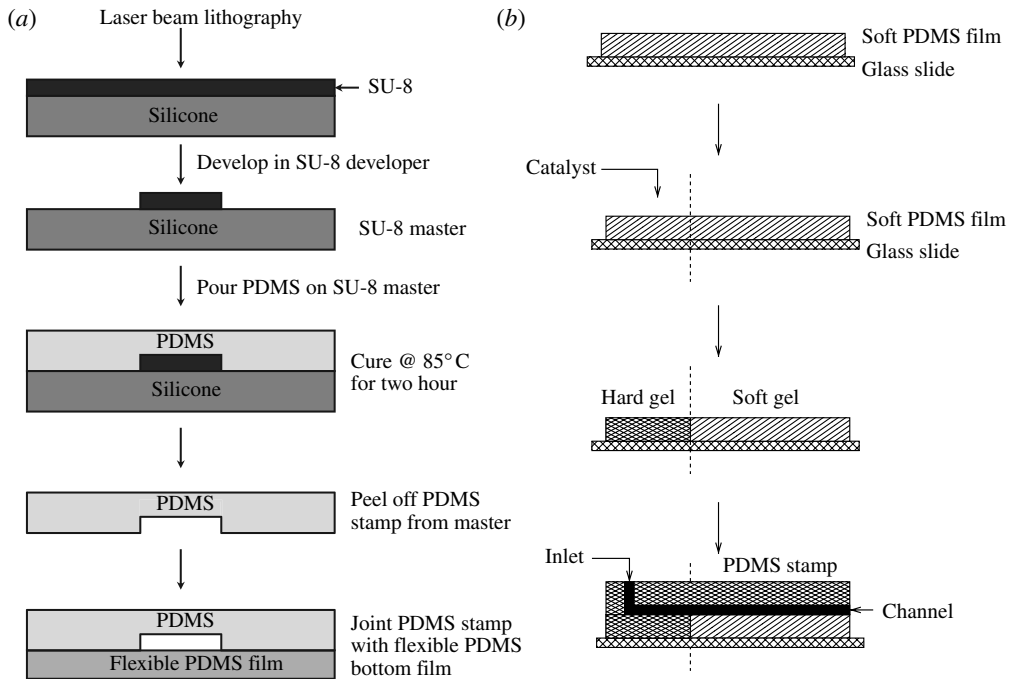


FIGURE 30. Cross-sectional view of the preparation of PDMS stamp using SU-8 lithography and its bonding onto the soft film to form the channel (a) and side view of fabrication of soft film, addition of catalyst to form hard section and its bonding with hard PDMS stamp to form the channel (b).

Instead, we first mix the monomer with catalyst of the concentration required for the soft section. The mixture is cast in the form of a film of thickness 2 mm on a glass plate, as shown in the top two figures in figure 30(b). After casting the film, additional catalyst is poured only in the developing section, so that only the developing section becomes hard, while the test section (where there is no additional catalyst) is soft, as shown in the third figure from top in figure 30(b). After fabrication of the two parts, the hard section shown as prepared in figure 30 is pressed onto the soft film, after a thin film of pre-polymer is added at the junction to bond the two sides, as shown in the bottom figure in figure 30(b). The entire assembly is then cured to obtain a micro-channel which has a development section with four hard walls and a test section with three hard walls and one soft wall.

The variation of the shear and compression moduli with catalyst concentration was determined as follows. At the time of making the soft wall, an additional slab of gel with the same catalyst concentration of size 2 cm × 2 cm and thickness 2 mm was prepared. This slab was placed on the bottom plate of the parallel plate geometry in an AR 1000N rheometer. The top plate was lowered until contact is made with the gel, and the storage and loss modulus were determined as a function of the frequency of oscillations using standard software. The compression modulus was determined by lowering the top plate and measuring the increase in the normal stress with compression. The spectrum of the storage modulus $G'(\omega)$ is shown as a function of frequency in figure 31(a). The loss modulus has also been measured in order to characterize the gel completely, and the magnitudes were similar to those calculated

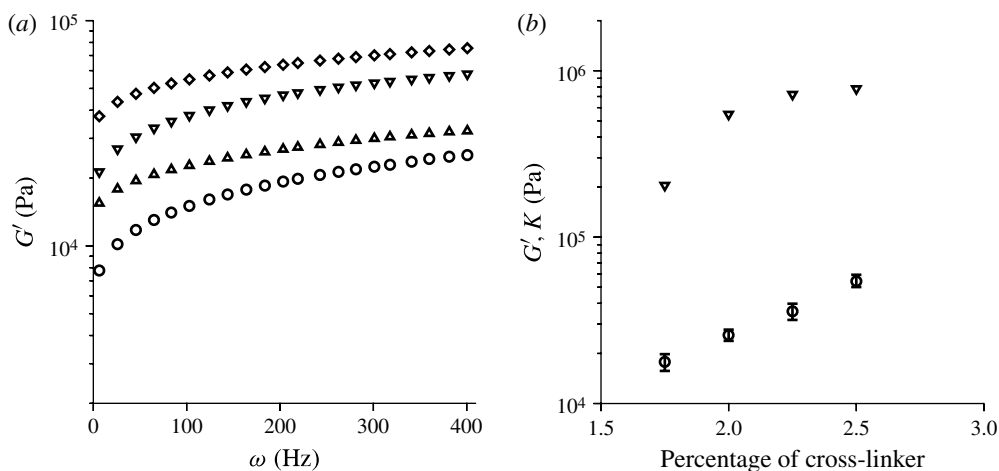


FIGURE 31. The storage modulus as a function of frequency (a) for gels with catalyst concentration 1.75 % (○), 2.00 % (△), 2.25 % (▽) and 2.50 % (◇); and (b) the plateau storage modulus G' (○) and the compression modulus K (▽) as a function of catalyst concentration. The error bars in (b) are over measurements for three independent samples with the same catalyst concentration.

earlier in Verma & Kumaran (2012). The average shear modulus is calculated by averaging over the plateau in the frequency range between 100 and 400 Hz in the spectra. The dependence of the average shear modulus (with error bars over three independent samples) and the compression modulus on the catalyst concentration is shown in figure 31(b). The compression modulus is found to be higher than the shear modulus by more than a factor of 10, indicating that the resistance to shear deformation is much smaller than that to volumetric compression or expansion. Thus, the gel can be considered an incompressible medium to a good approximation, and it can be parameterized by just the shear modulus alone. This enables us to use the constitutive relations for an incompressible solid in the following analytical methods section to carry out the linear stability analysis.

Appendix B. Validation of CFD procedure

Here, the simulation procedure is validated for a rectangular cross-section with length 4 cm, width 1.5 mm and height 100 μm , which corresponds to the dimensions of the undeformed channel. The configuration and coordinate system are shown in figure 32(a). A plug flow velocity profile is specified at the inlet, and a constant pressure is specified at the outlet in all the simulations. The grid spacing in the simulations, which is 20 μm in all directions, is the same as that used in §5 for the deformed channel. The results for the velocity profiles were obtained at four cross-sections separated by 1 cm each. These were found to be identical to within less than 0.2 %, indicating that the flow is fully developed. The profiles of the velocity scaled by the average velocity (ratio of flow rate and cross-sectional area) in the cross-section 1 cm from the entrance at different spanwise locations are shown in figure 32(b). These results are compared with the results obtained by a separation-of-variables procedure for the fully developed flow in a channel of rectangular cross-section, where 40 basis functions (sine functions in the cross-stream direction) were used in the

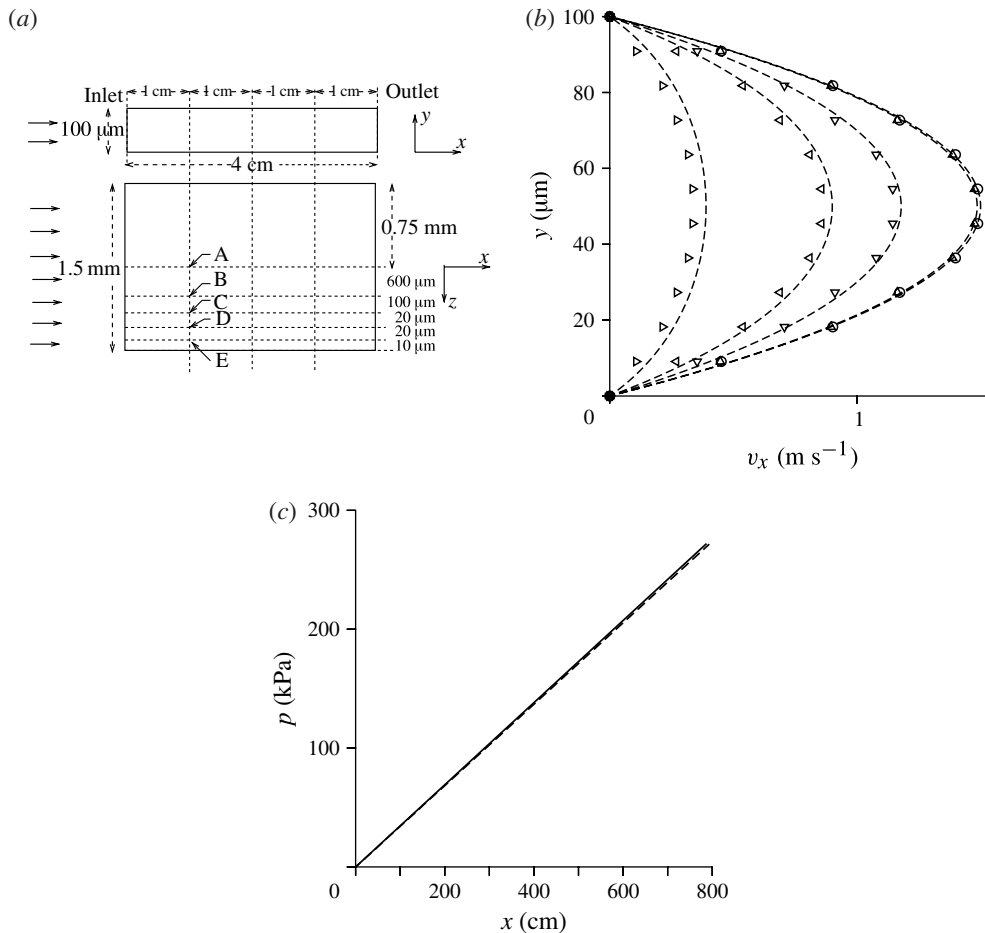


FIGURE 32. The elevation (top) and plan (bottom), not to scale, of the channel used for validation (a); the profiles of the velocity scaled by the average velocity at a Reynolds number of 300 based on the flow rate equation (2.1) at a distance 1 cm from the inlet (b) at different spanwise locations, \circ along the central plane at location A in (a) which is 750 μm from the wall, \triangle at location B 150 μm from the wall, ∇ at location C 50 μm from the wall, \triangleleft at location D 30 μm from the wall and \triangleright at location E 10 μm from the wall; and (c) the pressure difference across the channel as a function of the Reynolds number. In (b), the symbols are the simulation results and the lines are the results obtained using the separation-of-variables procedure for a fully developed flow in the channel. In (c), the solid line is the simulation result and the dashed line is the result obtained using the separation-of-variables procedure for a fully developed flow in the channel.

expansion for the velocity. There is very good agreement to within 1 %, between the simulations and analytical results even at a location 150 μm from the wall. Closer to the wall, there is a difference of $\sim 2\%$ at a distance of 50 μm from the wall, $\sim 3.5\%$ at a distance of 30 μm from the wall and $\sim 12\%$ at a distance of 10 μm from the wall. The difference in the velocity profiles at a distance of 10 μm from the wall is expected, because the distance from the wall is equal to one half of the grid spacing. When the distance from the wall is greater than the grid spacing, the results in figure 32(b) shows that there is excellent agreement between the simulations and analytical results.

The pressure difference across the channel from the simulations is compared with the theoretical results for a fully developed flow obtained by separation of variables in figure 32(c). Here, too, it is found that there is excellent agreement between the theoretical and simulation results, thereby confirming that the flow dynamics is well captured using a grid spacing of 20 μm for this configuration.

REFERENCES

- AHMED, D., MAO, X., SHI, J., JULURI, B. & HUANG, T. 2009 A millisecond micromixer via single-bubble-based acoustic streaming. *Lab on a Chip* **9**, 2738–2741.
- BAZANT, M. Z. & SQUIRES, T. M. 2004 Induced-charge electro-kinetic phenomena: theory and microfluidic applications. *Phys. Rev. Lett.* **92**, 066101.
- BESSOTH, F., DE MELLO, A. J. & MANZ, A. 1999 Microstructure for efficient continuous flow mixing. *Anal. Commun.* **36**, 213–215.
- BIRD, R. B., STEWART, W. E. & LIGHTFOOT, E. N. 2007 *Transport Phenomena*. John Wiley & Sons.
- BOYD, J. P. 1989 *Chebyshev and Fourier Spectral Methods*. Springer.
- CHOKSHI, P. P. & KUMARAN, V. 2008 Weakly nonlinear analysis of viscous instability in flow past a neo-Hookean surface. *Phys. Rev. E* **77**, 056303.
- CHOKSHI, P. P. & KUMARAN, V. 2009 Weakly nonlinear stability analysis of a flow past a neo-Hookean solid at arbitrary Reynolds numbers. *Phys. Fluids* **21**, 014109.
- DRAZIN, P. G. & REID, W. H. 2004 *Hydrodynamic Stability*. Cambridge University Press.
- EGGERT, M. D. & KUMAR, S. 2004 Observations of instability, hysteresis, and oscillation in low-Reynolds-number flow past polymer gels. *J. Colloid Interface Sci.* **278**, 234–242.
- GANAN-CALVO, A. M., FERRERA, C., TORREGROSA, M., HERRADA, M. A. & MARCHAND, M. 2011 Experimental and numerical study of the recirculation flow inside a liquid meniscus focused by air. *Microfluid Nanofluid* **11**, 65–74.
- GASTER, M. 1962 A note on the relation between temporally-increasing and spatially-increasing disturbances in hydrodynamic stability. *J. Fluid Mech.* **14**, 222–224.
- GAURAV, & SHANKAR, V. 2009 Stability of fluid flow through deformable neo-Hookean tubes. *J. Fluid Mech.* **627**, 291–322.
- GAURAV, & SHANKAR, V. 2010 Stability of pressure-driven flow in a deformable neo-Hookean channel. *J. Fluid Mech.* **659**, 318–350.
- GERVAIS, T., EL-ALI, J., GUNTHERB, A. & JENSEN, K. F. 2006 Flow-induced deformation of shallow microfluidic channels. *Lab on a Chip* **6**, 500–507.
- GKANIS, V. & KUMAR, S. 2005 Stability of pressure driven creeping flows in channels lined with a nonlinear elastic solid. *J. Fluid Mech.* **524**, 357–375.
- GLASGOW, I. & AUBRY, N. 2003 Enhancement of microfluidic mixing using time pulsing. *Lab on a Chip* **3**, 114–116.
- GORDILLO, J. M., CHENG, Z., GANAN-CALVO, A. M., MARQUEZ, M. & WEITZ, D. A. 2004 A new device for the generation of microbubbles. *Phys. Fluids* **16**, 2828–2834.
- HARDY, B. S., UECHI, K., ZHEN, J. & KAVEHPOUR, H. P. 2009 The deformation of flexible PDMS microchannels under a pressure driven flow. *Lab on a Chip* **9**, 935–938.
- HOF, B., JUEL, A. & MULLIN, T. 2003 Scaling of the turbulence transition threshold in a pipe. *Phys. Rev. Lett.* **91**, 244502.
- JIANG, F., DRESE, K. S., HARDT, S., KUPPER, M. & SCHONFELD, F. 2004 Helical flows and chaotic mixing in curved micro channels. *AIChE J.* **50**, 2297–2305.
- KANE, A. S., HOFFMANN, A., BAUMGARTEL, P., SECKLER, R., REICHARDT, G., HORSLEY, D. A., SCHULER, B. & BAKAJIN, O. 2008 Microfluidic mixers for the investigation of rapid protein folding kinetics using synchrotron radiation circular dichroism spectroscopy. *Analyt. Chem.* **80**, 9534–9541.
- KNIGHT, J. B., VISHWANATH, A., BRODY, J. P. & AUSTIN, R. H. 1998 Hydrodynamic focusing on a silicon chip: mixing nanoliters in microseconds. *Phys. Rev. Lett.* **80**, 3863–3866.

- KRINDEL, P. & SILBERBERG, A. 1979 Flow through gel-walled tubes. *J. Colloid Interface Sci.* **71**, 39–50.
- KUMARAN, V. 1995 Stability of the viscous flow of a fluid through a flexible tube. *J. Fluid Mech.* **294**, 259–281.
- KUMARAN, V. 1996 Stability of an inviscid flow in a flexible tube. *J. Fluid Mech.* **320**, 1–17.
- KUMARAN, V. 1998 Stability of fluid flow in a flexible tube at intermediate Reynolds number. *J. Fluid Mech.* **357**, 123–140.
- KUMARAN, V., FREDRICKSON, G. H. & PINCUS, P. 1994 Flow induced instability at the interface between a fluid and a gel at low Reynolds number. *J. Phys. France II* **4**, 893–911.
- KUMARAN, V. & MURALIKRISHNAN, R. 2000 Spontaneous growth of fluctuations in the viscous flow of a fluid past a soft interface. *Phys. Rev. Lett.* **84**, 3310–3313.
- LEE, M. G., CHOI, S. & PARK, J.-K. 2010 Rapid multivortex mixing in an alternately formed contraction-expansion array microchannel. *Biomed. Microdevices* **12**, 1019–1026.
- LEE, S., KIM, D., LEE, S. & KWON, T. 2006 A split and recombination micromixer fabricated in a PDMS three-dimensional structure. *J. Micromech. Microengng* **16**, 1067–1074.
- LIU, R. H., STREMLER, M. A., SHARP, K. V., OLSEN, M. G., SANTIAGO, J. G., ADRIAN, R. J., AREF, H. & BEEBE, D. J. 2000 Passive mixing in a three-dimensional serpentine microchannel. *J. Microelectromech. Syst.* **9**, 190–197.
- MENSING, G. A., PEARCE, T. M., GRAHAM, M. D. & BEEBE, D. J. 2004 An externally driven magnetic micro-stirrer. *Phil. Trans. R. Soc. Lond. A* **362**, 1059–1068.
- MURALIKRISHNAN, R. & KUMARAN, V. 2002 Experimental study of the instability of the viscous flow past a flexible surface. *Phys. Fluids* **14**, 775–780.
- POSNER, J. & SANTIAGO, J. J. 2006 Convective instability of electrokinetic flows in a cross-shaped microchannel. *J. Fluid Mech.* **555**, 1–42.
- SCHMID, P. J. & HENNINGSON, D. S. 1994 Optimal energy density growth in Hagen-Poiseuille flow. *J. Fluid Mech.* **277**, 197–225.
- SHANKAR, V. & KUMARAN, V. 1999 Stability of non-parabolic flows in a flexible tube. *J. Fluid Mech.* **395**, 211–236.
- SHANKAR, V. & KUMARAN, V. 2000 Stability of non-axisymmetric modes in a flexible tube. *J. Fluid Mech.* **407**, 291–314.
- SHANKAR, V. & KUMARAN, V. 2001a Asymptotic analysis of wall modes in a flexible tube revisited. *Eur. Phys. J. B* **19**, 607–622.
- SHANKAR, V. & KUMARAN, V. 2001b Weakly nonlinear stability of viscous flow past a flexible surface. *J. Fluid Mech.* **434**, 337–354.
- SHANKAR, V. & KUMARAN, V. 2002 Stability of wall modes in the flow past a flexible surface. *Phys. Fluids* **14**, 2324–2338.
- SHRIVASTAVA, A., CUSSLER, E. L. & KUMAR, S. 2008 Mass transfer enhancement due to a soft elastic boundary. *Chem. Engng Sci.* **63**, 4302–4305.
- STROOCK, A. D., DERTINGER, S. K. W., AJDARI, A., MEZIC, I., STONE, H. A. & WHITESIDES, G. M. 2002 Chaotic mixer for microchannels. *Nature* **295**, 647–651.
- SUTTERBY, J. L. 1965 Finite difference analysis of viscous laminar converging flow in conical tubes. *Appl. Sci. Res. A* **15**, 241–252.
- THAOKAR, R. M., SHANKAR, V. & KUMARAN, V. 2001 Effect of tangential interface motion on the viscous instability in fluid flow past flexible surfaces. *Eur. Phys. J. B* **23**, 533–550.
- TREFETHEN, L. N., TREFETHEN, A. E., REDDY, S. C. & DRISCOLL, T. A. 1993 Hydrodynamic stability without eigenvalues. *Science* **261**, 578–584.
- VERMA, M. K. S. & KUMARAN, V. 2012 A dynamical instability due to fluid-wall coupling lowers the transition Reynolds number in the flow through a flexible tube. *J. Fluid Mech.* **705**, 322–347 2012.
- WEIDEMAN, J. A. & REDDY, S. C. 2000 A Matlab differentiation matrix suite. *ACM Trans. Math. Softw.* **26**, 465519.
- YANG, C., GRATTONI, C. A., MUGGERIDGE, A. H. & ZIMMERMAN, R. W. 2000 A model for steady laminar flow through a deformable gel-coated channel. *J. Colloid. Interface Sci.* **266**, 104–111.